Crucial Role of Structural Design on Performance of Cryogel-based EMI Shields: An Experimental Review

Sara Rostami [1], Ahmadreza Ghaffarkhah [1,2], Seyyed Alireza Hashemi [1], Stefan Wuttke [3,4], Orlando J. Rojas [2,5,6], Mohammad Arjmand [1]*

[1]Nanomaterials and Polymer Nanocomposites Laboratory, School of Engineering, University of British Columbia, Kelowna, BC, V1V 1V7, Canada

[2]Bioproducts Institute, Department of Chemical & Biological Engineering, The University of British Columbia, 2360 East Mall, Vancouver, BC, V6T 1Z3, Canada

[3] Basque Centre for Materials, Applications & Nanostructures (BCMaterials), Bld. Martina Casiano, 3rd. Floor UPV/EHU Science Park Barrio Sarriena s/n, Leioa, 48940 Spain

[4] IKERBASQUE, Basque Foundation for Science, Bilbao, 48013, Spain

[5] Department of Chemistry, 2036 Main Mall. Vancouver, The University of British Columbia, Vancouver, BC Canada V6T 1Z1.

[6] Department of Wood Science, The University of British Columbia, 2900-2424 Main Mall Vancouver, BC Canada V6T 1Z4.

Corresponding Author: **mohammad.arjmand@ubc.ca**

1. Characterization of Graphene Oxide

Various analyses were performed to characterize the synthesized graphene oxide (GO) and confirm its successful synthesis with the desired functionalities. Fig. S1a demonstrates the FESEM images of GO, indicating its 2D morphology. The HRTEM images also confirm the 2D morphology of large flake GO with favorable exfoliation during the synthesis process (Fig. S1b-c). The X-ray diffractogram of GO flakes is depicted in Fig. S1d, showing a well-defined sharp peak at 2θ of $10.64°$ with an inter-layer spacing of 8.31 Å, corresponding to the (001) crystalline plane of GO. The expansion of the d-spacing, compared to pristine graphite with a d-spacing of 3.4 Å, arises from the presence of oxygen-based functional groups on GO. These functional groups influence the separation distance between the layers of GO.

Fig. 1e illustrates the two well-defined peaks of micro-Raman spectroscopy of GO at 1343 and 1581 cm^{-1} corresponding to the D-band and G-band of GO flakes. This spectroscopy showcased an I_D/I_G ratio of 0.86, confirming the controlled rate of defects and high quality of the synthesized GO flakes. Fig. S1f, further confirms the synthesis of GO with typical functional groups, i.e., C–O ($\sim$1061 cm^{-1}), C–O–C ($\sim$1223 cm^{-1}), C–OH ($\sim$1396 cm^{-1}), C=C double bonds carbon atoms ($\sim$1631 cm^{-1}), carbonyl (C=O) moieties ($\sim$1738 cm^{-1}), and hydroxyl (–OH) functional groups ($\sim$3398 cm^{-1}). The EDS analysis of GO also indicates the homogenous distribution of 70.9 wt% carbon and 29.1 wt% oxygen elements at the surface of GO (Fig. S2).

2. Electromagnetic Interface Shielding

2.1. Shielding Background

Electromagnetic waves (EMWs), characterized by synchronized oscillations of electric and magnetic fields, interact with the surface or interior of the shield through three primary pathways:

reflection, absorption, and multiple reflections. Furthermore, due to certain morphological designs and material choices, another shielding phenomenon called multiple internal reflections or internal scattering may also occur in materials with numerous internal interfaces, such as cryogels, further increasing the electromagnetic interference (EMI) shielding capability of a structure.[1, 2]

Conductive shields exhibit lower impedance compared to free space, preventing the propagation of incident waves within the shield.[1] This results in the transfer of energy from the incident EMWs to free-charged particles and electrons in the shield, causing them to oscillate and create an induced or scattered field known as reflection. This reflection primarily occurs at the surface of the shield and is largely influenced by the electrical conductivity of the shielding structures. Alongside reflection, a portion of EMWs dissipates as heat upon interaction with EMI shielding materials, a mechanism known as absorption. This is the desired outcome of an EMI shielding system achieved through smart structural design and material selection. [3] Additionally, a portion of incident EMWs may pass through the shielding materials, termed transmission.[1, 4]

Multiple reflections occur within thin EMI shielding films, where incident EMWs reflect back and forth between the front and back interfaces of the shield.[5] This process continues until the incident wave loses all its energy, which can reduce the EMI shielding capability of the shields as it allows a portion of EMWs to escape the shielding material. The effectiveness of multiple reflections depends on the thickness of the shield. It becomes less significant when the shield's thickness approaches or exceeds the skin depth, the distance beneath the shield's front surface where the electric field intensity decreases to 1/e of the incident wave's intensity. Conversely, if the shield thickness is less than the skin depth, multiple reflections can reduce the shielding effectiveness of the structure.[1, 6, 7]

Internal scattering or internal multiple reflections occur within materials with numerous internal

interfaces or designed porosities, such as cryogels, xerogels, aerogels, foams, and multi-layered shields. Unlike multiple reflections, internal scattering can enhance shielding performance by promoting absorption through back-and-forth reflections between impedance-mismatched interfaces. This increases the absorption rate of the shield, contributing to the absorption mechanism.[1, 8]

It is critical to distinguish internal scattering from multiple reflections. Internal scattering involves numerous internal interfaces within the shield that trap and dissipate EMWs in the form of heat through back-and-forth reflections between impedance-mismatched interfaces. Multiple reflections, on the other hand, refer to reflections between the front and back interfaces of a thin film shield, reducing shielding effectiveness by allowing infiltrated EMWs to escape.[1, 6, 9, 10]

Our research primarily focuses on strategies to enhance the internal porosities of GO-based cryogels with diverse porosities as a result of varying fabrication methods. This approach investigates the effect of trapped EMWs within the cryogels' structure and internal scattering by facilitating back-and-forth reflections between impedance-mismatched surfaces on EMI effectiveness. In the following section, detailed discussions on formulations and EMI shielding parameters will be presented.

2.2. Shielding Setup

The EMI shielding capability of conductive as-developed graphene-based cryogels was evaluated using a two-port VNA. This method involves sending a signal from port one (S_1) with a defined frequency to the sandwiched sample between WR-90 waveguide adaptors attached to VNA via microwave cables. The receiver detects the transmitted (S_{21}) and reflected (S_{11}) waves, measuring both the magnitude and phase data of each received signal. The same procedure is repeated from port two (S_2), where the system sends the signal to the sample at the same frequency, measuring

the transmitted (S_{12}) and reflected (S_{22}) waves by the receiver on the opposite side. This measurement procedure is repeated for each frequency increment. The transmission and reflection measurements are provided as complex scattering parameters (S_{11}, S_{12}, S_{21}, and S_{22}). These scattering parameters, shielding mechanisms, and employed formulations will be discussed in the following sections.

2.3. Shielding Formulations

Subsequently, after obtaining the complex scattering parameters, the transmittance (T), reflectance (R), and absorbance (A) of the shields were determined utilizing the following equations:

$$T = |S_{12}|^2 = |S_{21}|^2 \qquad (1)$$

$$R = |S_{22}|^2 = |S_{11}|^2 \qquad (2)$$

$$A = 1 - R - T \qquad (3)$$

Other shielding characteristics of samples, including absorption loss (SE_A) and reflection loss (SE_R) were measured as follows:

$$SE_A = 10log\frac{1-R}{T} \qquad (4)$$

$$SE_R = 10log\frac{1}{1-R} \qquad (5)$$

Where R represents reflectance (as per equation 2) and T stands for transmittance (as per equation 1). According to Schelkunoff's theory, the overall EMI shielding effectiveness (SE_T) of the samples is determined by combining the absorption loss, reflection loss, and the multiple reflections loss ($SE_T = SE_R + SE_A + SE_M$). [11-13]

The specific shielding effectiveness (SSE/t), serving as an indicator of shielding relative to the weight of a structure, was calculated as follows:

$$\text{SSE/t} = \frac{SE_T}{\rho.t} \tag{6}$$

Where SE_T represents the total shielding in dB, ρ is the density in g cm^{-3}, and t is the shield thickness in cm.
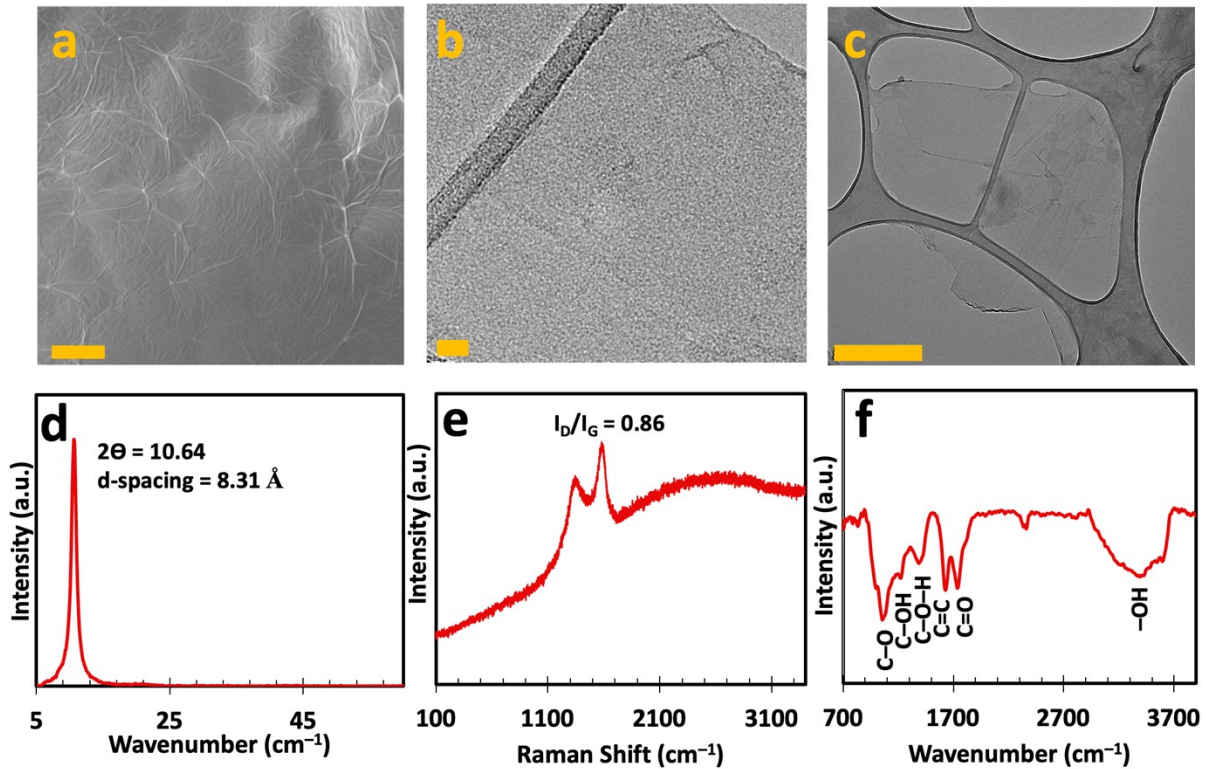
3. Figures and Tables

Figure S1. (a) FESEM images of GO flakes and (b-c) HRTEM. (d) XRD, (e) Raman, and (f) FTIR spectra of the synthesized GO. (b-c) Reproduced based on our previous open-access article according to the terms of the Creative Commons CC-BY-NC-ND license.[2] Copyright 2023, Springer Nature. Scale bars in (a), (b), (c) correspond to 20 μm, 20 nm, and 500 nm, respectively.
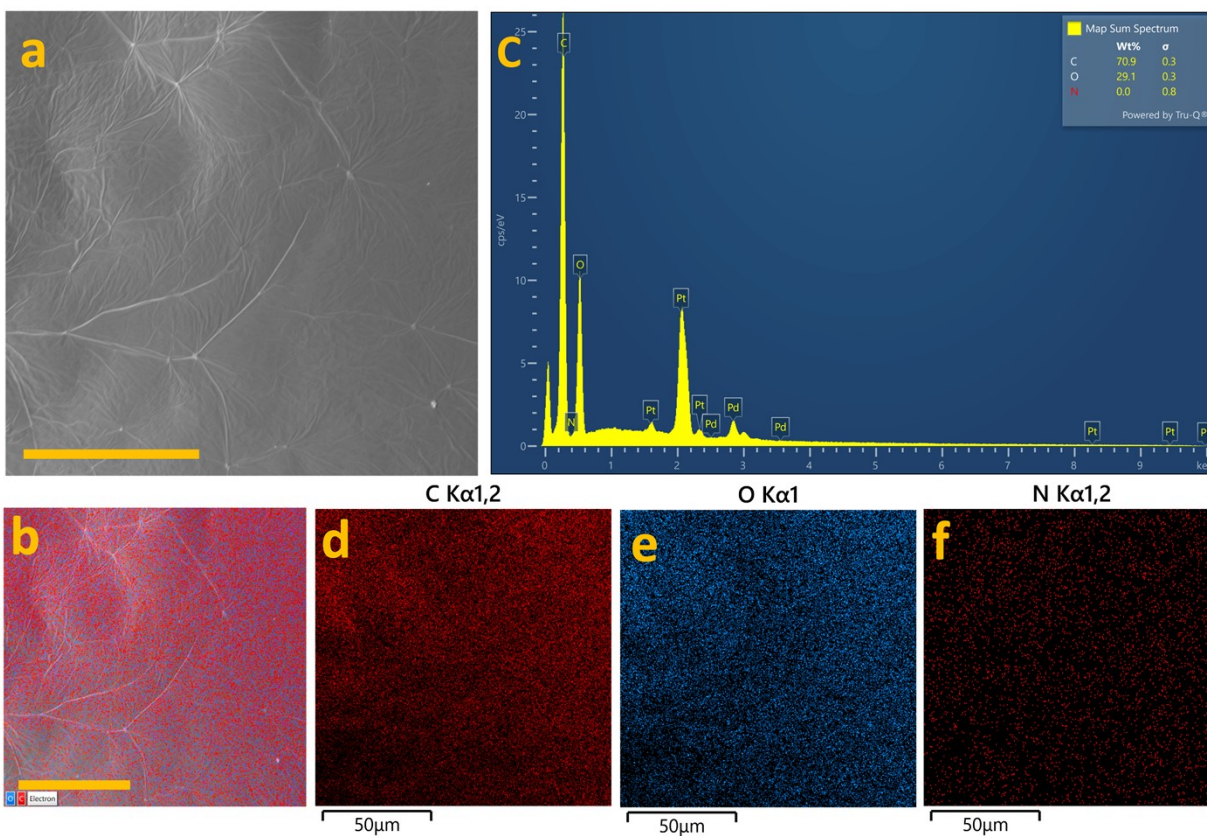
Figure S2. (a-b) FESEM image and EDS of the focused area. (c) EDS analysis of GO flakes along with the elemental distribution. (d-f) EDS mapping analysis of GO flakes. Scale bars in (a-b) correspond to 50 µm.
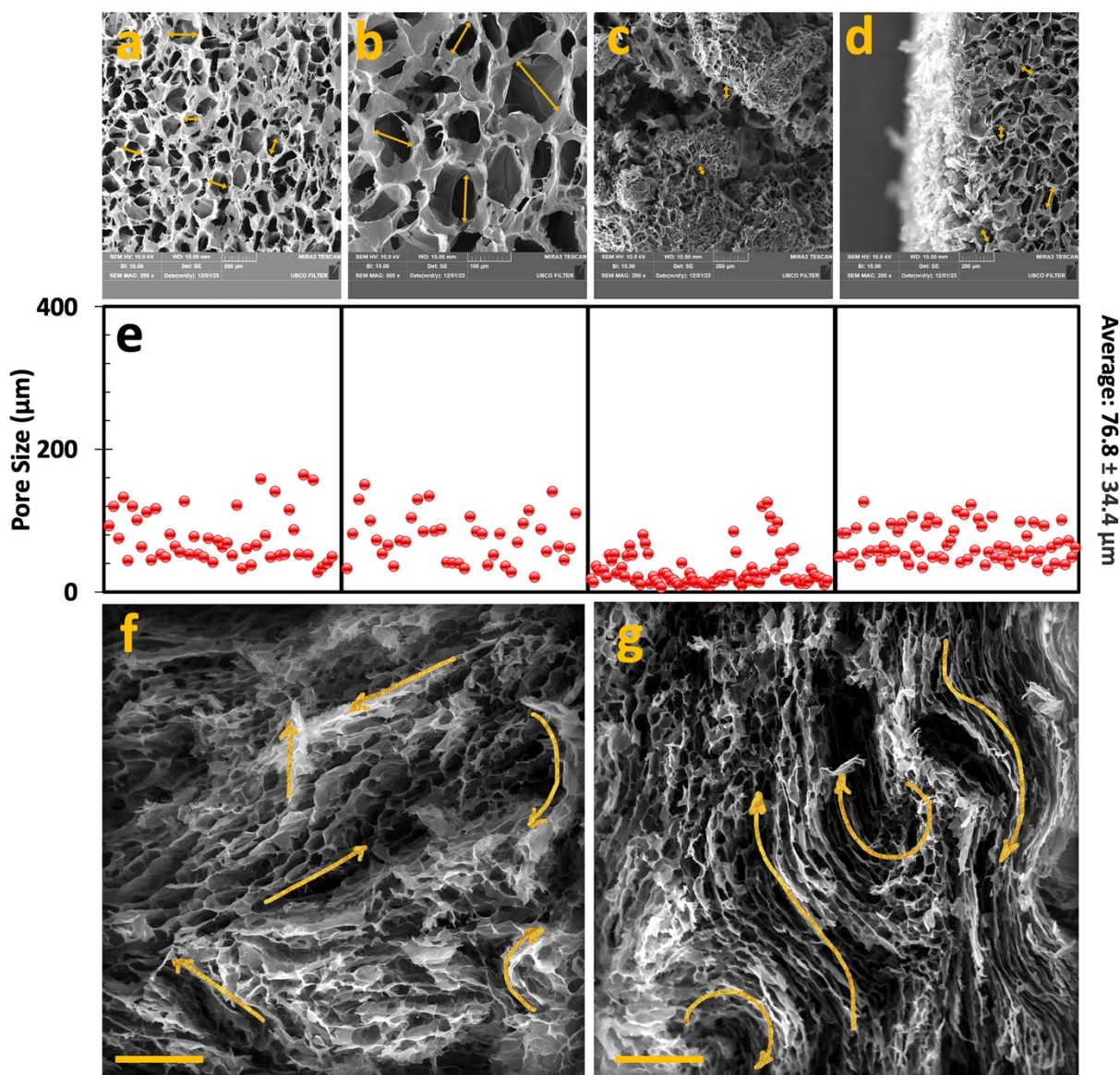
Figure S3. (a-d) Random selection of FESEM images was assessed to evaluate (e) the pore size distribution of direct-molded cryogels and their corresponding average size. The X-axis in (e) represents the data point numbers with no particular order. (f-g) FESEM images of direct-molded cryogels, representing random crystal formation due to disordered ice crystal formation in GO aqueous suspension. Scale bars in (f-g) correspond to 100 µm. The classification of pores was determined using ImageJ software based on SEM morphological assessments for pores>10 µm, and does not adhere to any standardized criteria or regulatory guidelines for porous materials.
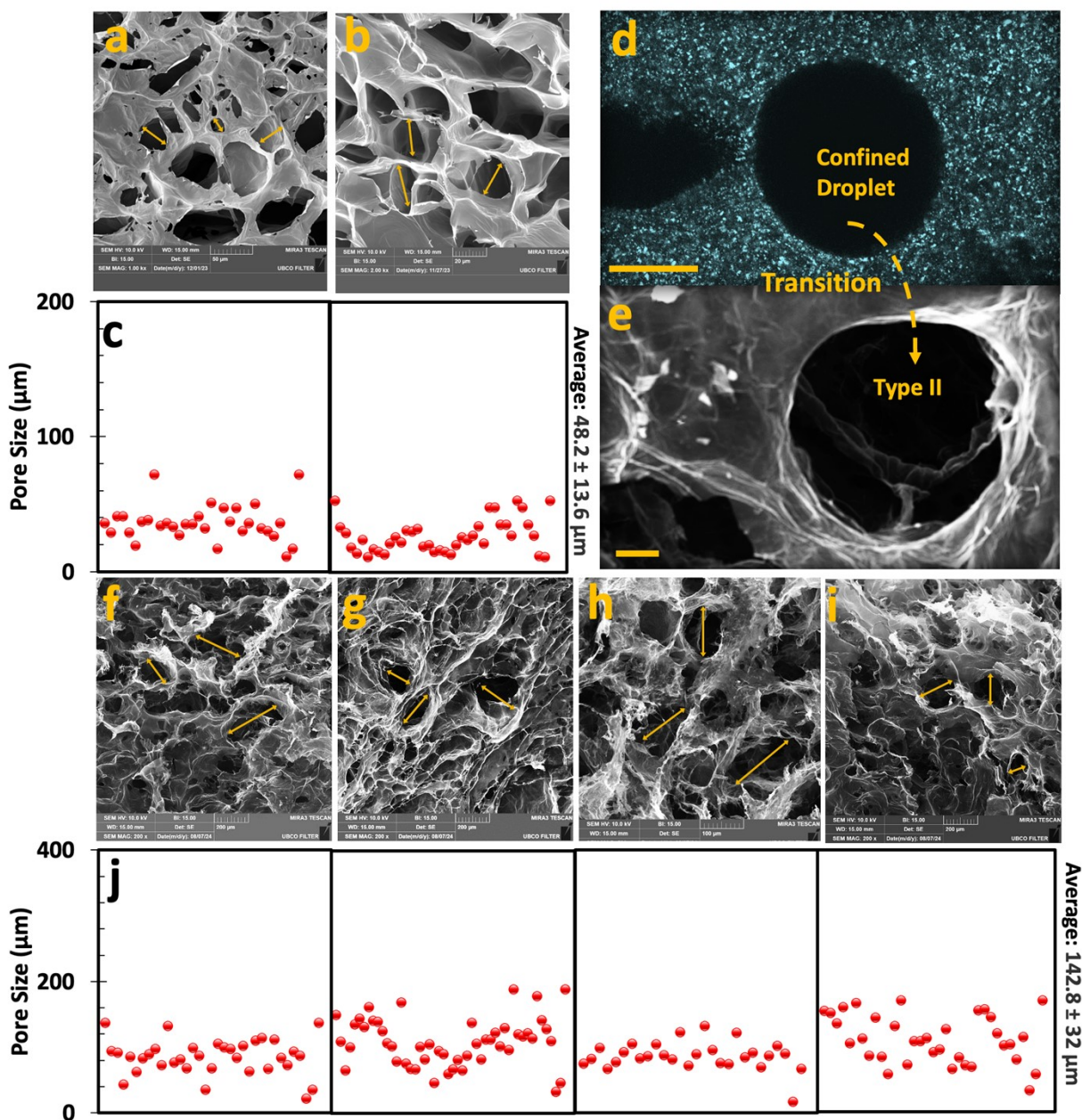
**Figure S4.** (a-b) Randomly selected FESEM images were used to analyze (e) the primary micro-scale pores present in emulsion-templated cryogels, which form due to ice crystal formation in the water phase of the Pickering emulsion during freezing and subsequent freeze-drying. (d) The confined hexane droplets within the Pickering emulsion act as templates, (e) resulting in larger voids within the final constructs, also known as secondary porosity. (f-i) FESEM images of emulsion-templated cryogels made from structured Pickering emulsions were used to evaluate (j) the distribution and average size of secondary pores in these cryogels (Type II). The X-axis in (c,

j) represents data point numbers with no particular order. Scale bars in (d-e) correspond to 50 µm. The classification of pores into two distinct types was determined using ImageJ software based on SEM morphological assessments for pores>10 µm, and does not adhere to any standardized criteria or regulatory guidelines for porous materials.
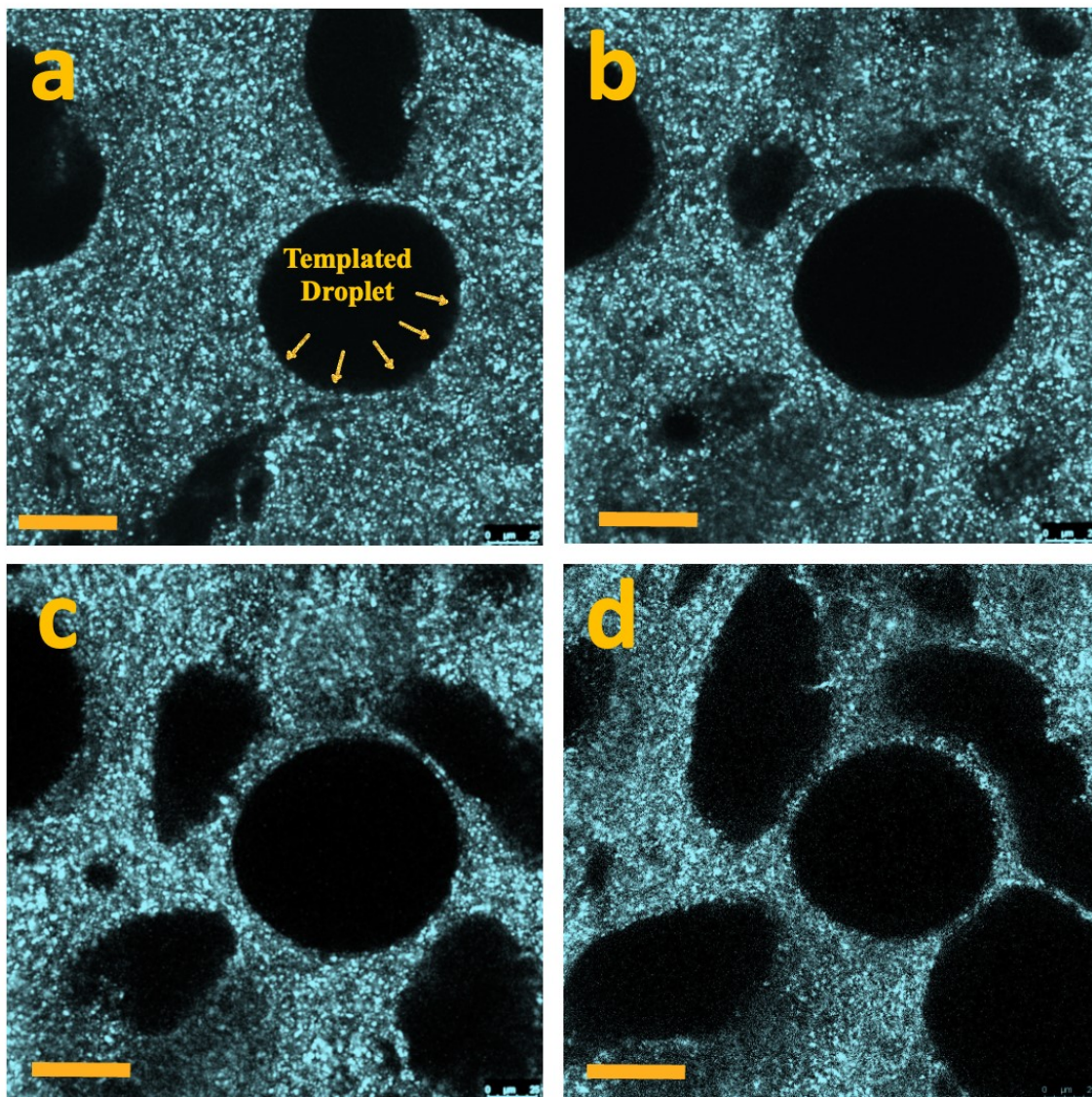
Figure S5. (a-d) Confocal images of oil-in-water Pickering emulsion, showcasing confined oil droplets in GO aqueous phase. All scale bars correspond to 50 µm.
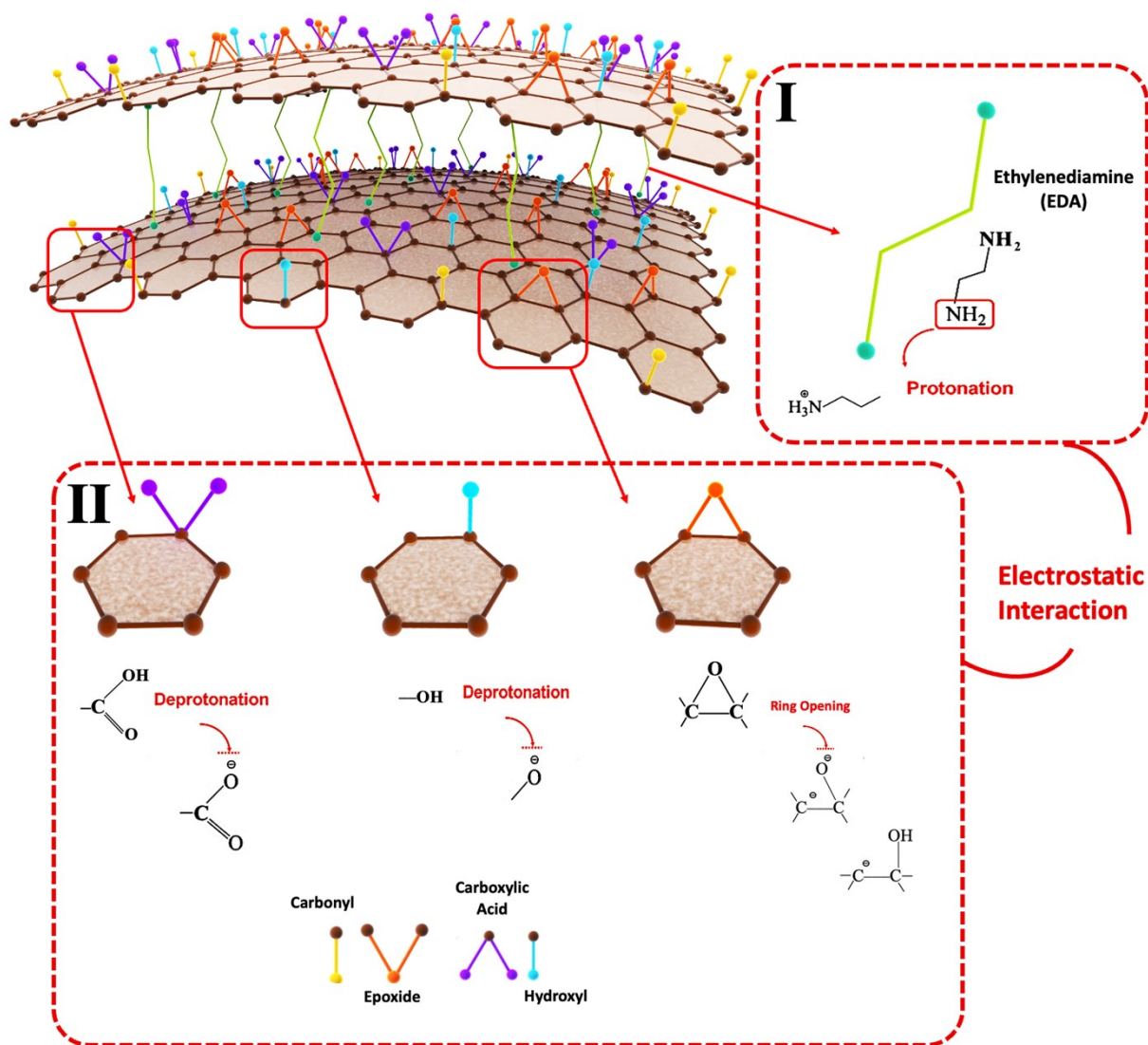
Figure S6. Anticipated mechanism for the cross-linking of GO sheets with EDA: The amine group of EDA is expected to electrostatically interact with the functional groups on GO: (I) The protonated amine group of EDA can react with (II) the carboxyl groups on GO, forming amide linkages and/or interacting with hydroxyl groups via hydrogen bonding. In some cases, EDA potentially opens the epoxy rings present on the GO surface, leading to the formation of secondary amine groups and hydroxyl groups.
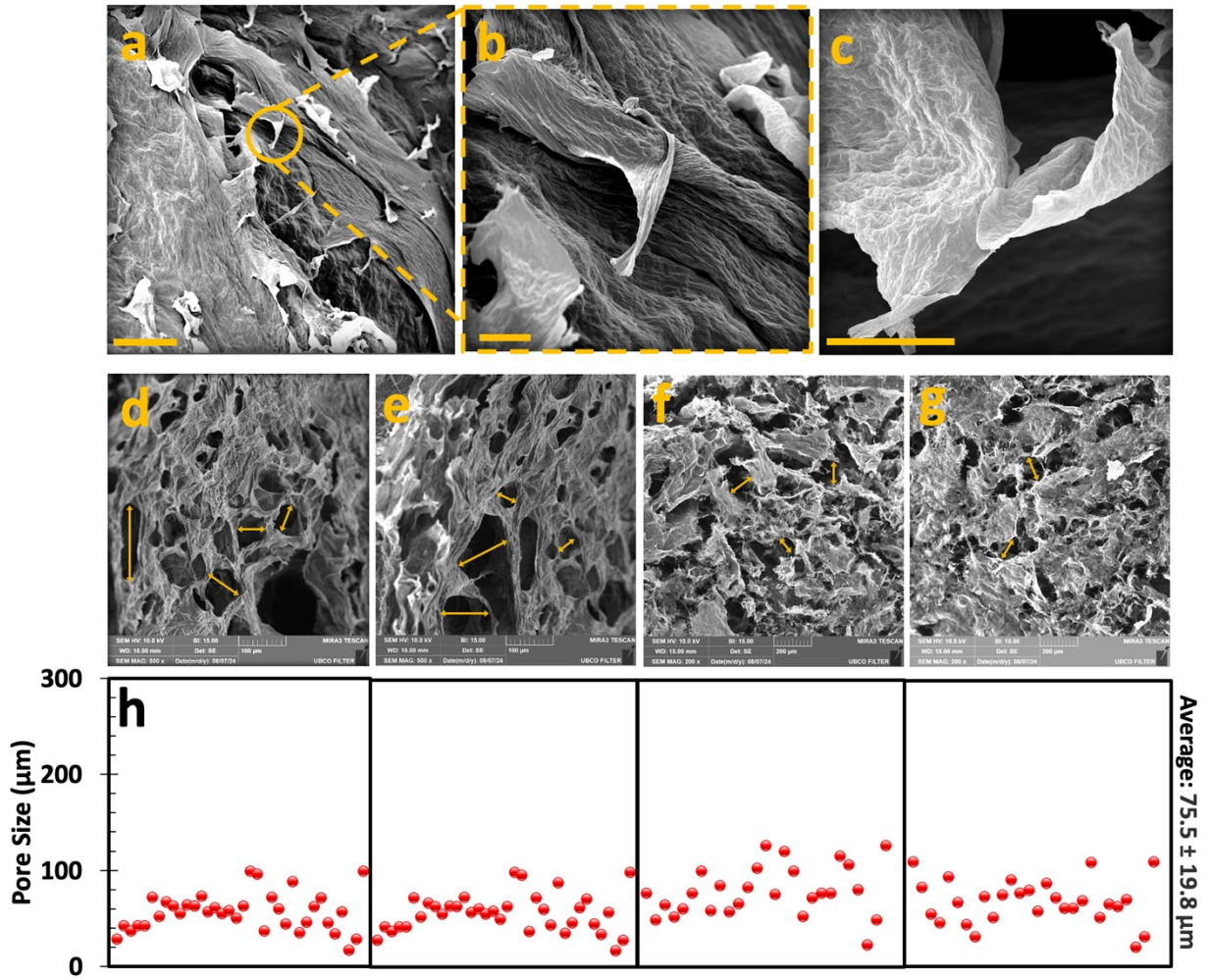
Figure S7. (a-c) FESEM images of chemically-crosslinked cryogels demonstrating folded and crumpled skin formed during the freezing process. (d-g) Randomly selected FESEM images were used to evaluate (h) the micro-scale pore distribution of chemically-crosslinked cryogels and their corresponding average size. The X-axis in (h) represents the data point numbers with no particular order. Scale bars in (a) and (b, c) correspond to 100 µm and 20µm, respectively. The classification of pores was determined using ImageJ software based on SEM morphological assessments for pores>10 µm, and it does not adhere to any standardized criteria or regulatory guidelines for porous materials.
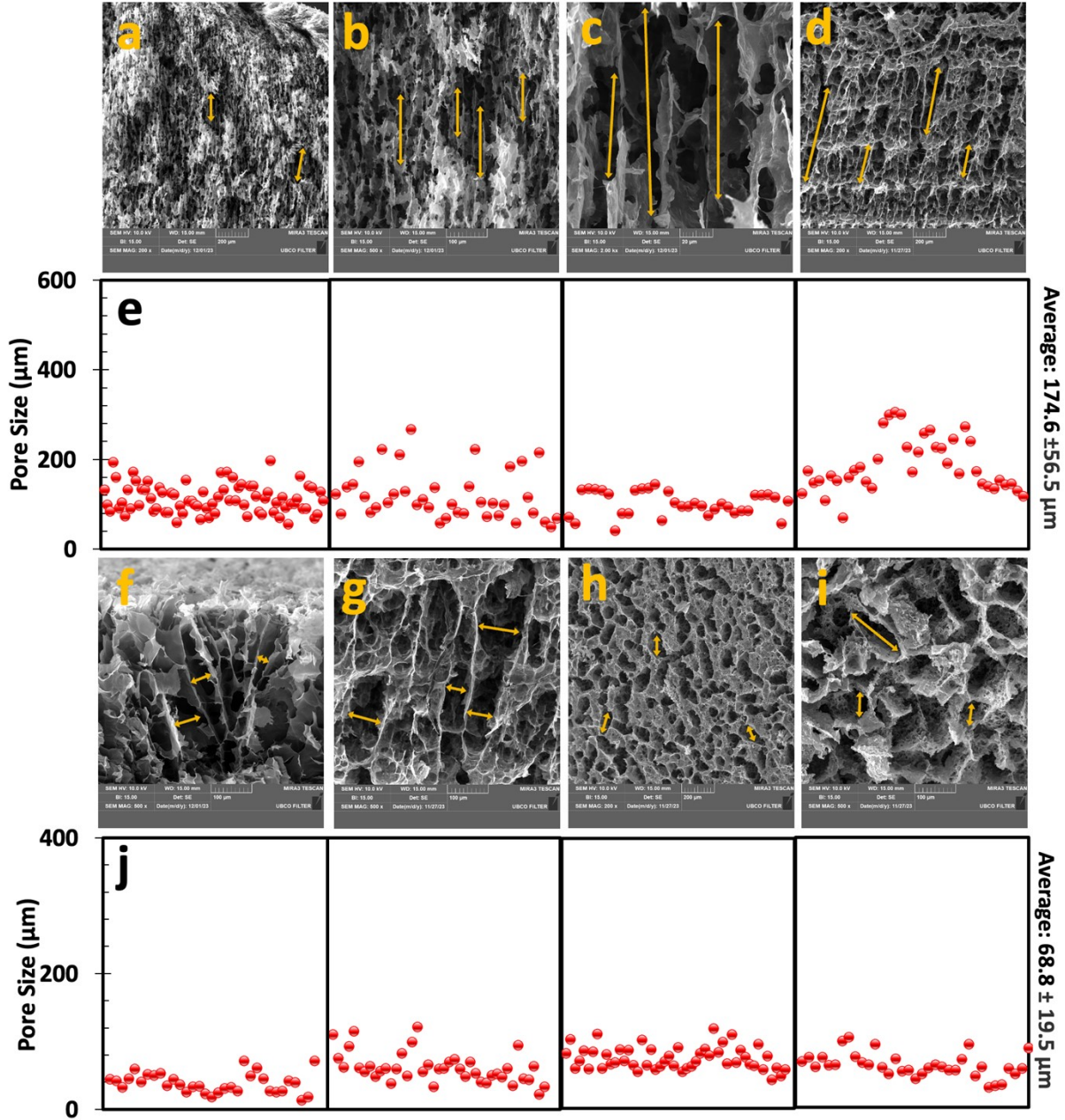
Figure S8. (a-d) FESEM images of the cross-sectional view of freeze-cast cryogels, indicating bottom-up ice crystal formation along the temperature gradient. (e) The corresponding pore distribution of freeze-cast cryogels and their average size. (f-g) Longitudinal and (h-i) top-view FESEM images of freeze-cast cryogels were assessed to evaluate (j) the transverse micro-scale pore distribution and their average size. The top view image confirms the successful ice-crystal nucleation and growth up to the surface. FESEM images are selected randomly for an unbiased evaluation. The X-axis in (e) and (j) represents the data point numbers with no particular order.

The classification of pores was determined using ImageJ software based on SEM morphological assessments for pores>10 µm, and it does not adhere to any standardized criteria or regulatory guidelines for porous materials.
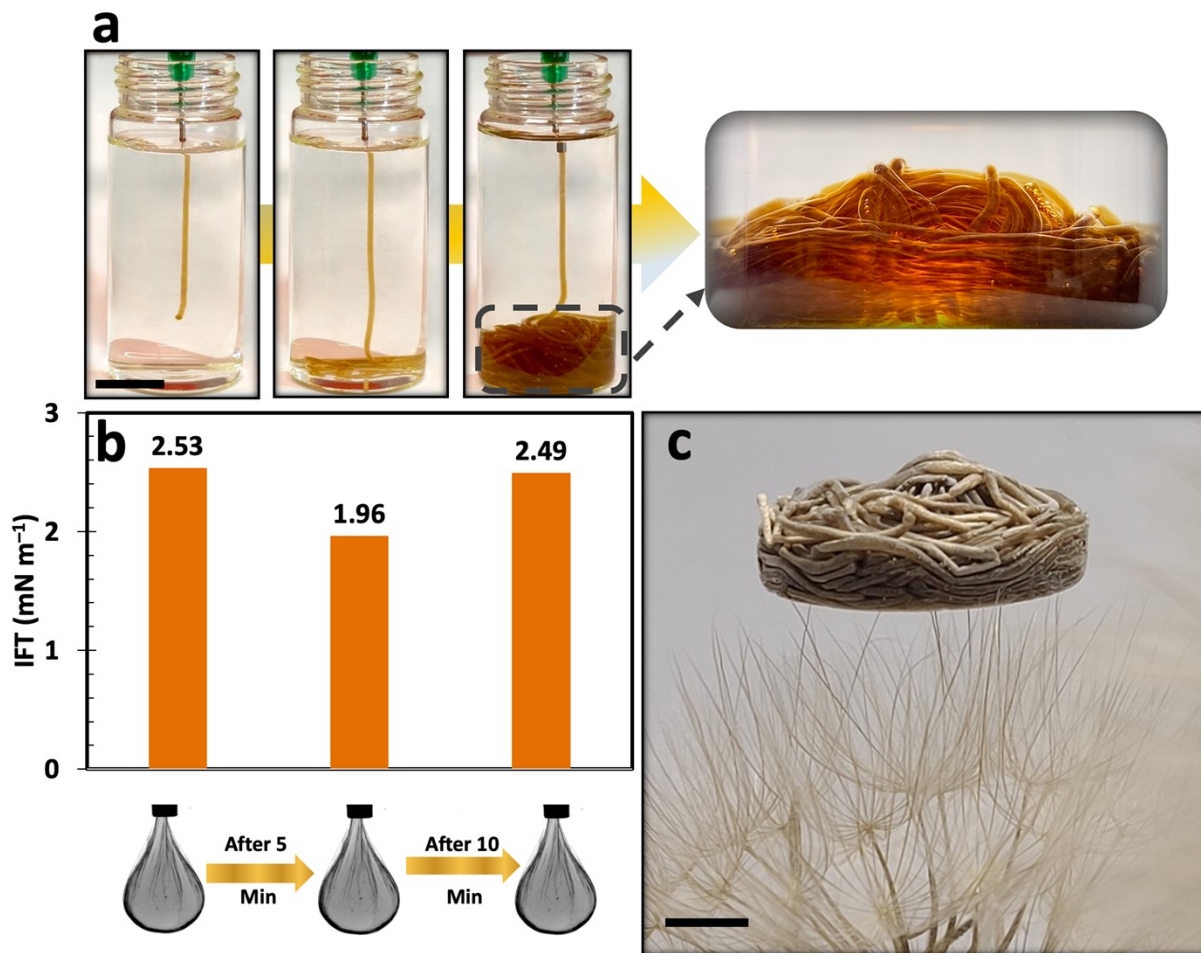
**Figure S9.** (a) Digital images demonstrating liquid-in-liquid streaming upon injection of ~ 10 mg ml^{-1} GO aqueous suspension into a nonpolar domain containing ligand. (b) A 5- and 10-min stability assessment of a 1 mg ml^{-1} GO pendant drop in hexane/POSS medium was measured. This test indicated that the nanoparticle surfactant jamming at the interface is stable and irreversible with almost the same IFT values, where the liquid is locked into a non-equilibrium shape even after 10 min, preserving the shape of the pendant with B-factor endorsement. (c) Digital images of ultra-lightweight worm-like cryogels after freezing and lyophilization on pappus. Scale bars in (a, c) correspond to 10 mm.
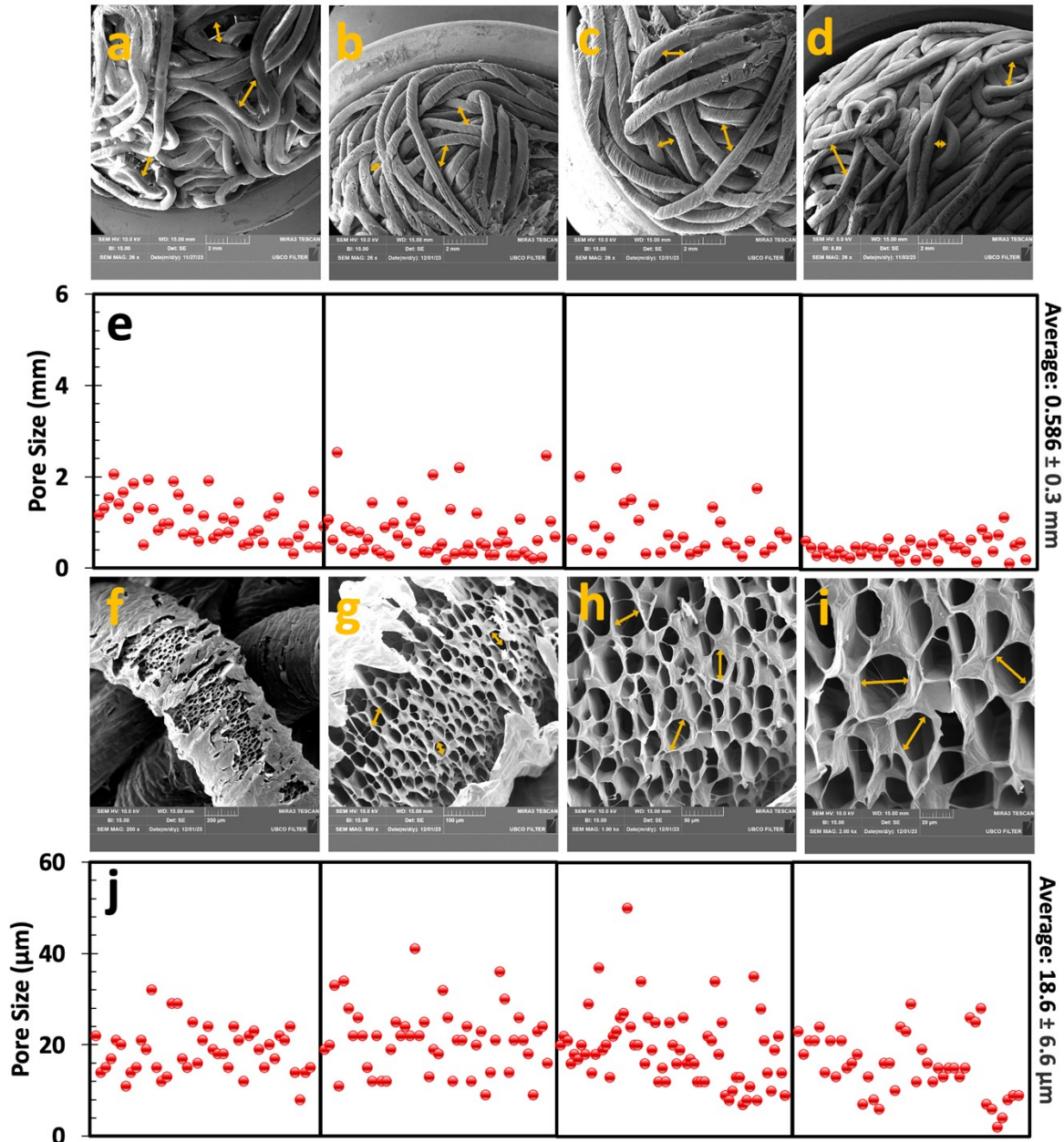
Figure S10. (a-d) FESEM images of worm-like cryogels were randomly selected to evaluate (e) the intra-space between the filaments, introduced as macro-scale porosity. (f-i) Micro-scale porosity within the core of the robust skin of the filaments, generated due to ice crystal formation during freezing within the tubular filament. (j) The corresponding distribution and the average size of the micro-pores. The X-axis in (e) and (j) represents the data point numbers with no particular order. The classification of pores into two distinct types was determined using ImageJ software based on SEM morphological assessments for pores>10 μm, and does not adhere to any standardized criteria or regulatory guidelines for porous materials.
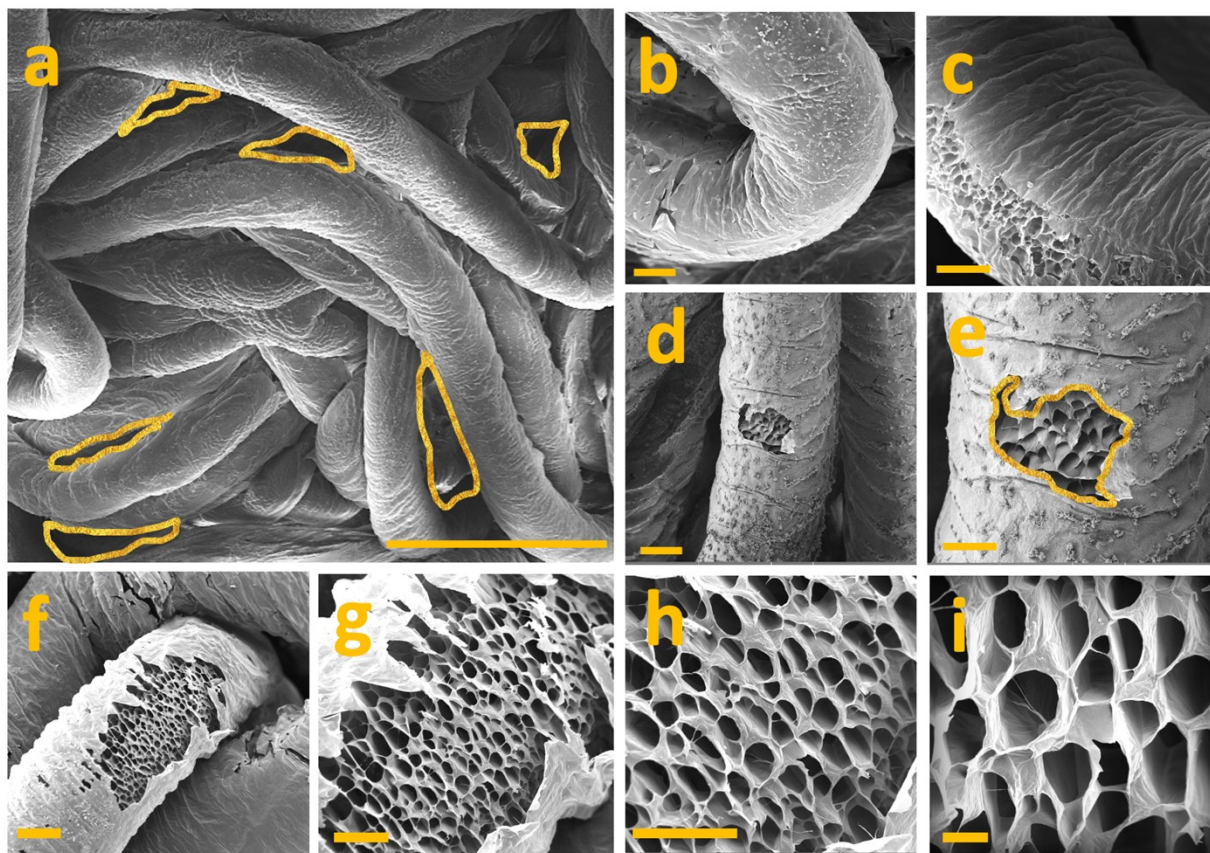
Figure S11. FESEM images of worm-like cryogels with dual porosity. (a-b) The macro-scale porosity forms due to freezing the streamed tubular filaments. (c-h) An interfacial skin dressed up a core with micro-scale porosity. This skin formed upon the jamming of nanoparticle surfactants at the interface. Scale bars in (a), (b, d, f), (c, e, g, h), and (i) correspond to 2mm, 200 μm, 100 μm, and 20 μm, respectively.
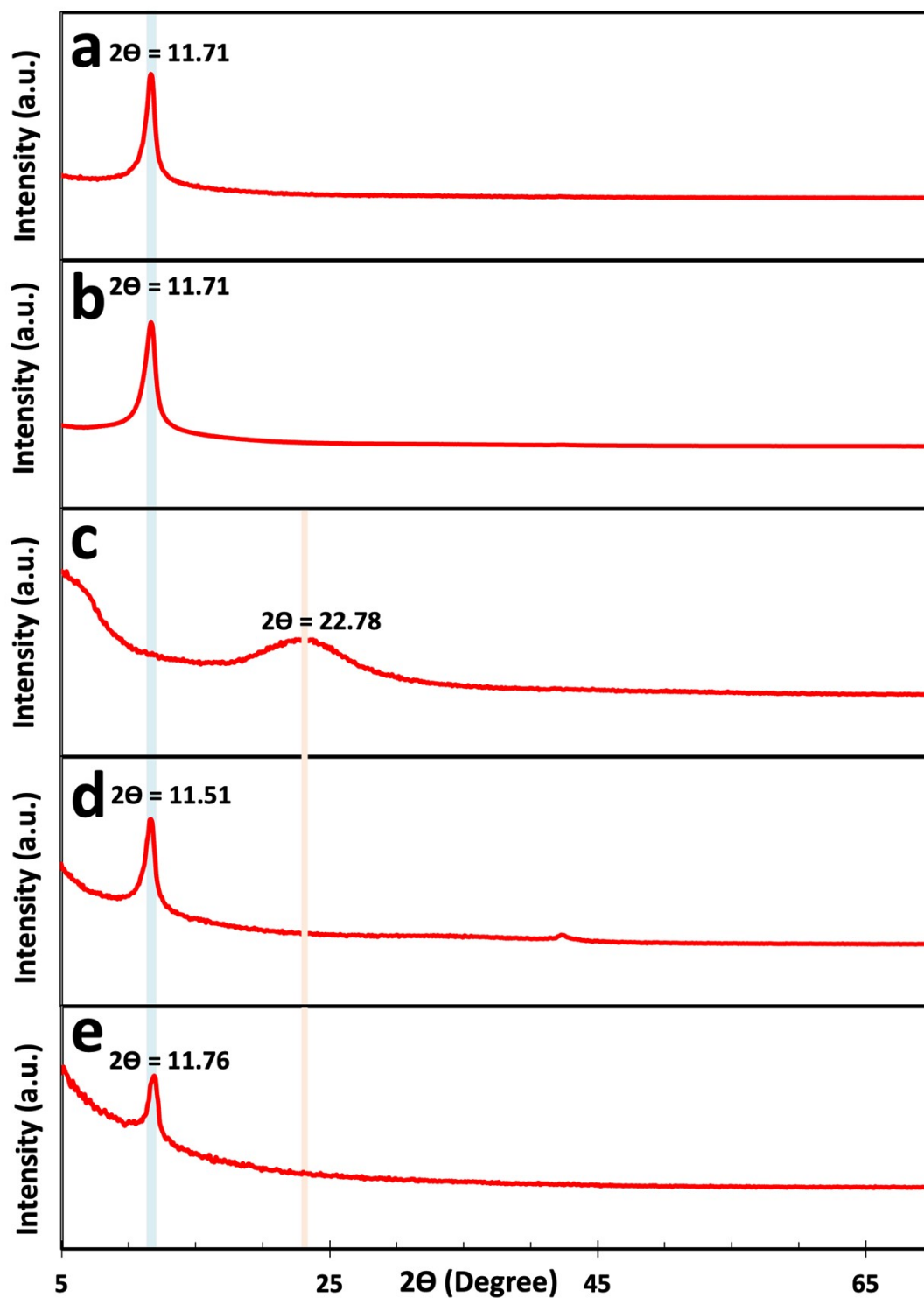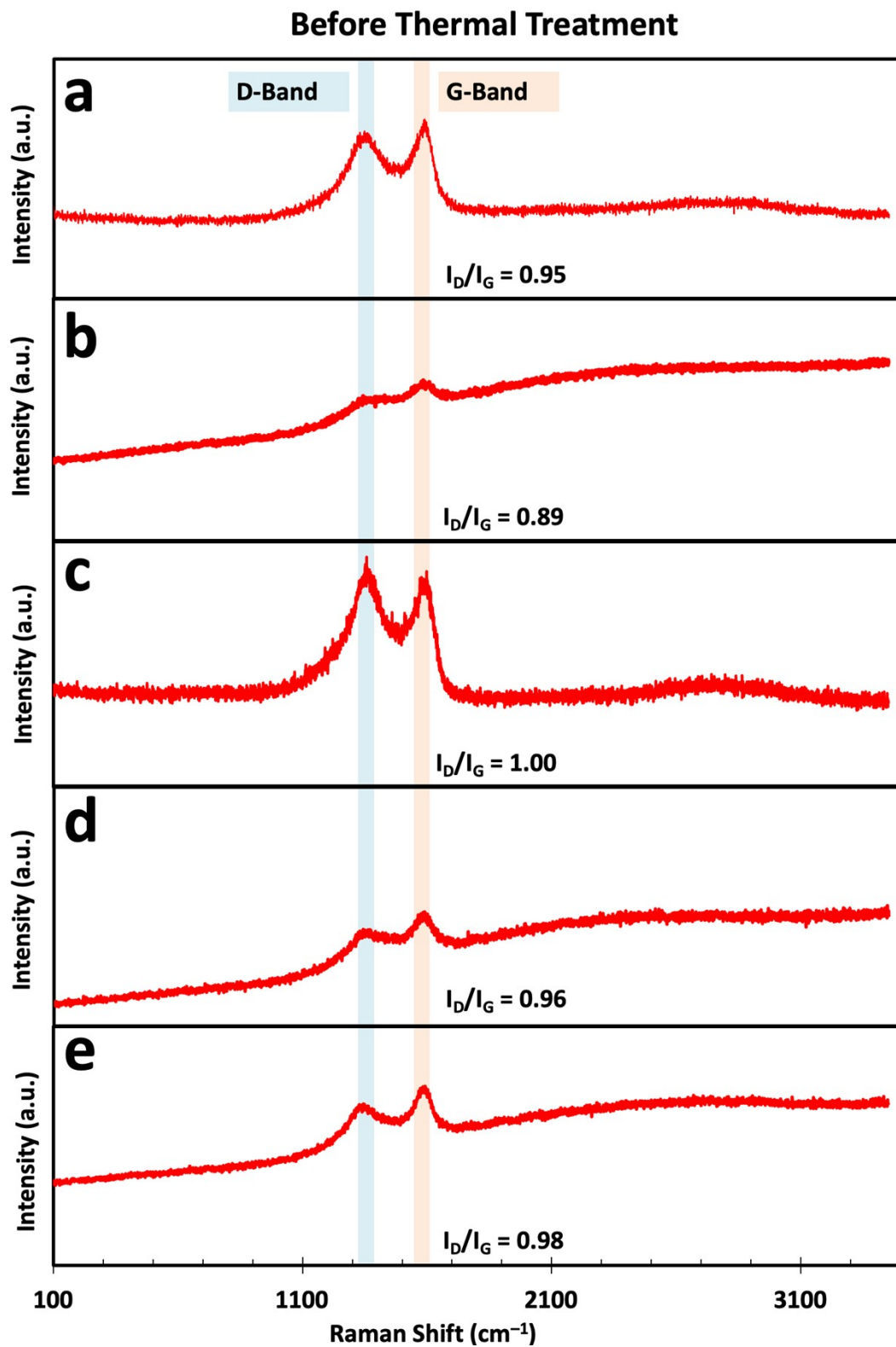
Before Thermal Treatment

Figure S12. X-ray diffractogram of (a) direct-molded, (b) emulsion-templated, (c) chemically-crosslinked, (d) freeze-cast, and (e) worm-like cryogels before thermal treatment.

After Thermal Treatment

a

$2\Theta = 26.51$

b

$2\Theta = 26.37$

c

$2\Theta = 25.78$

d

$2\Theta = 26.33$

e

$2\Theta = 26.21$

Intensity (a.u.)

5   25   2Θ (Degree)   45   65
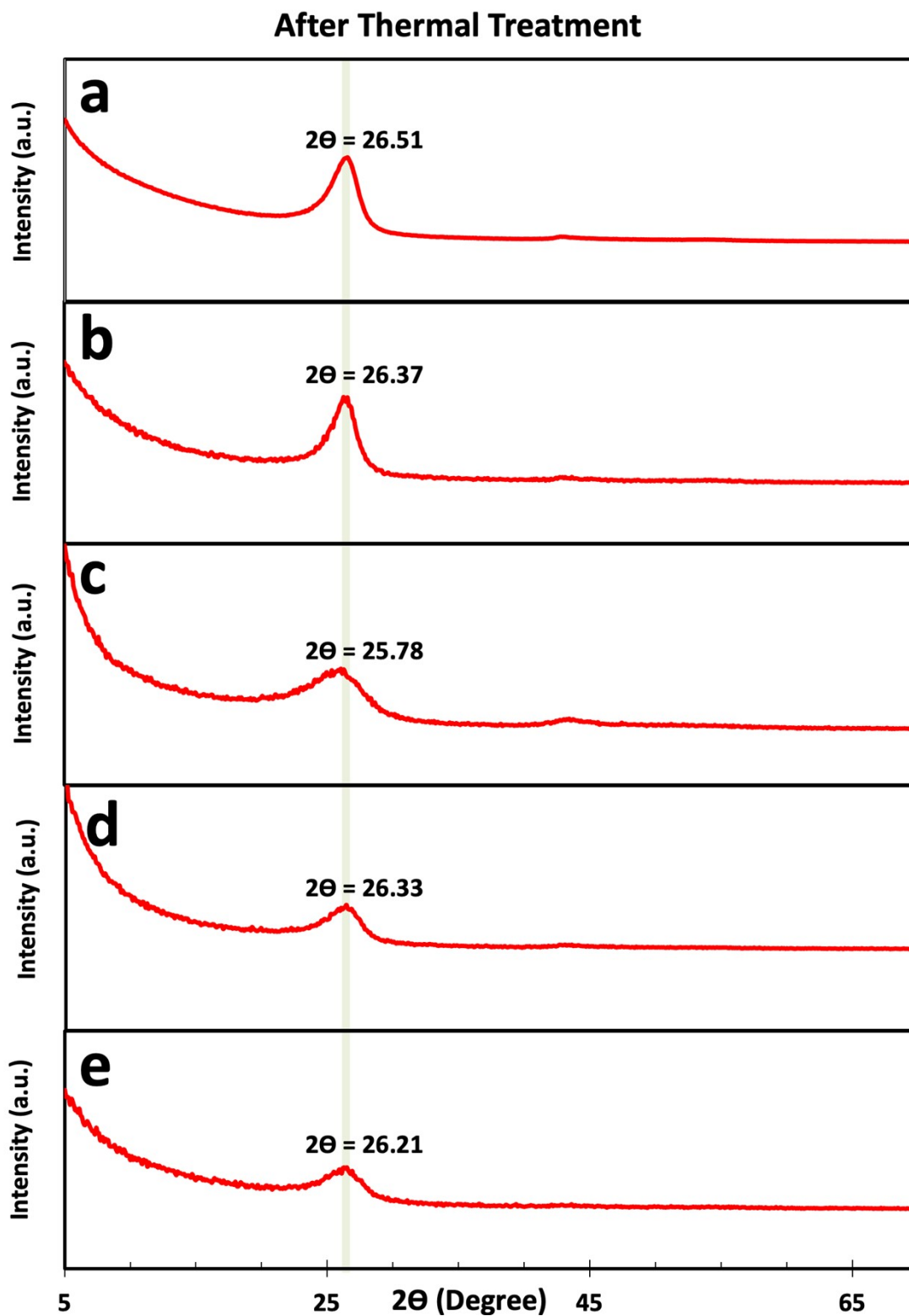
Figure S13. X-ray diffractogram of (a, f) direct-molded, (b, g) emulsion-templated, (c, h) chemically-crosslinked, (d, i) freeze-cast, and (e, j) worm-like cryogels after thermal annealing at 800°C under argon for 1 h.

Before Thermal Treatment

Figure S14. Micro-Raman spectra of (a) direct-molded, (b) emulsion-templated, (c) chemically-crosslinked, (d) freeze-cast, and (e) worm-like cryogels before thermal treatment.
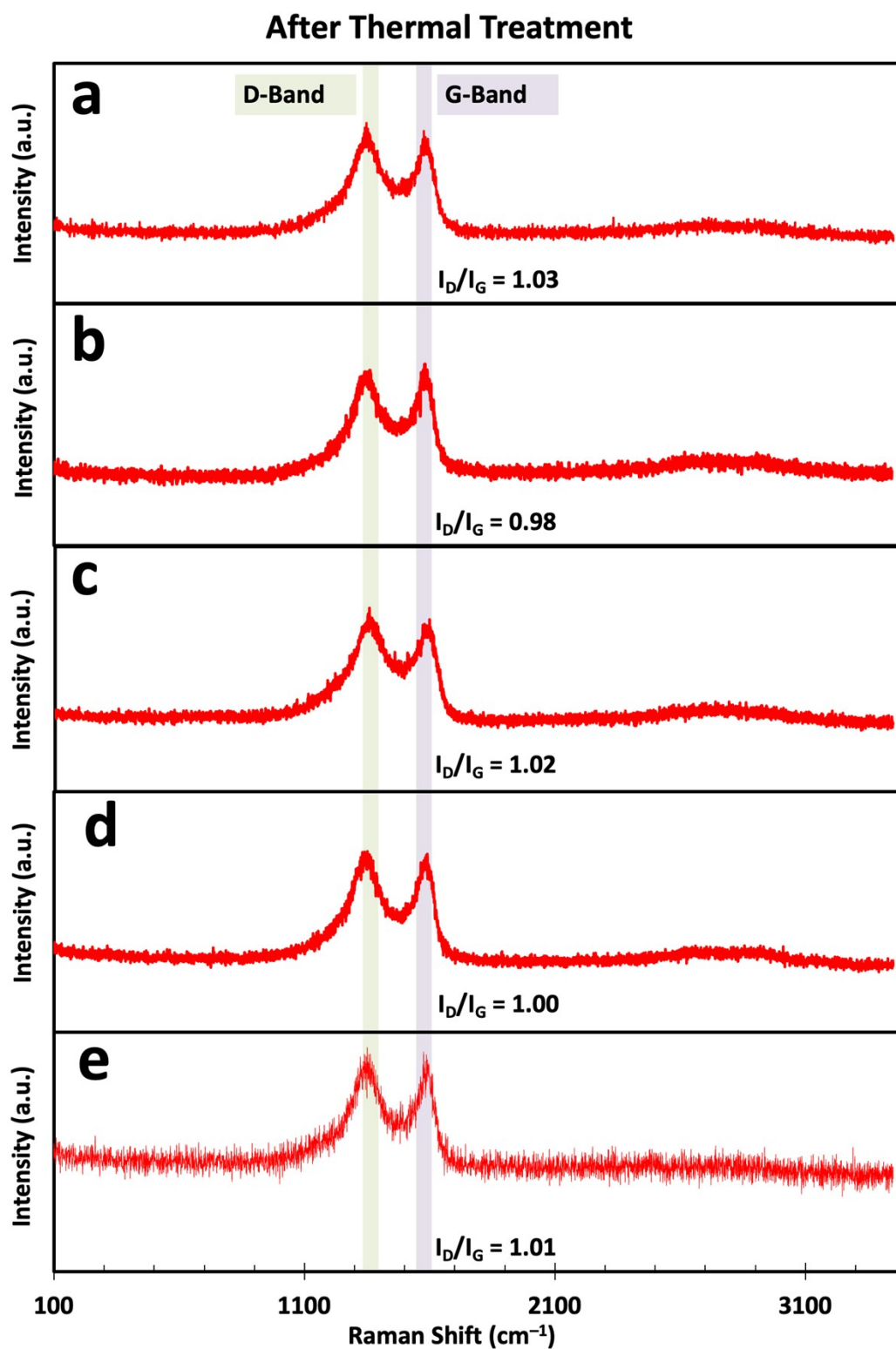
Figure S15. Micro-Raman spectra of (a) direct-molded, (b) emulsion-templated, (c) chemically-crosslinked, (d) freeze-cast, and (e) worm-like cryogels after thermal annealing at 800°C under argon for 1 h.
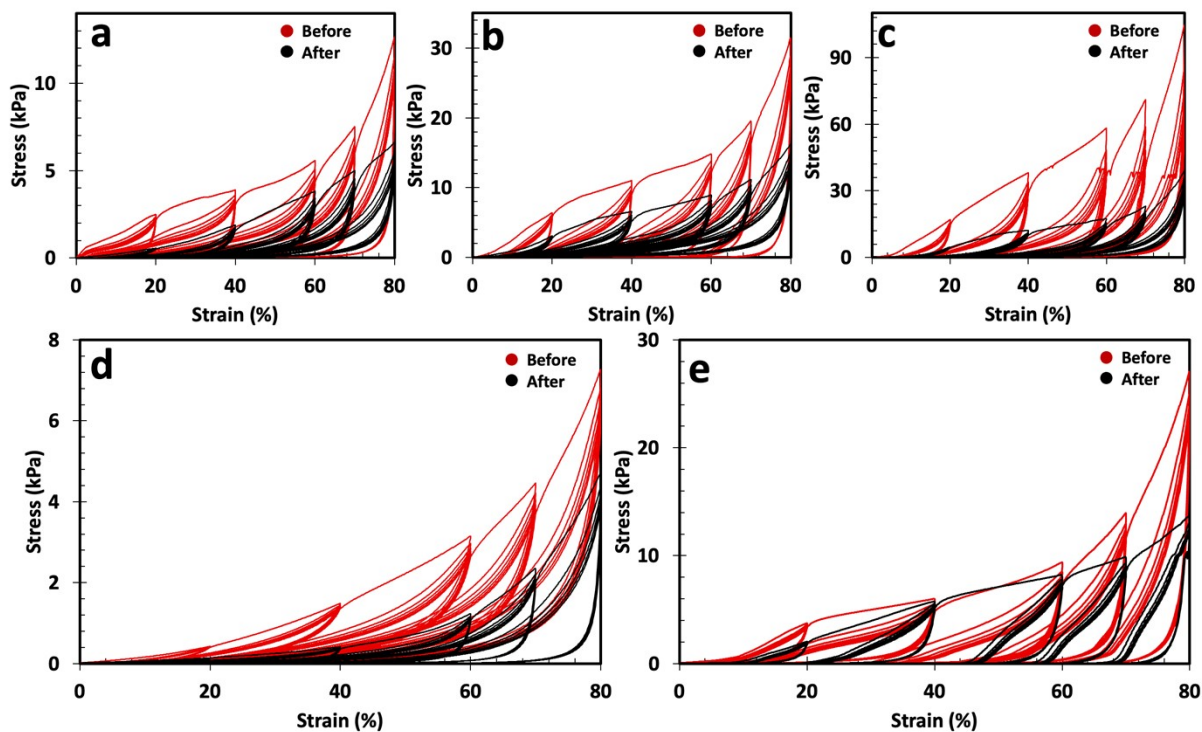
Figure S16. (a-e) The strain-stress curves of GO-based cryogels before and after thermal annealing fabricated through (a) direct molding, (b) emulsion templating, (c) chemically-induced gelation, (d) unidirectional freeze-casting, and (e) liquid-in-liquid templating. The cyclic compression test was conducted at 20, 40, 60, 70, and 80% of compressive strains over repeated cycles.
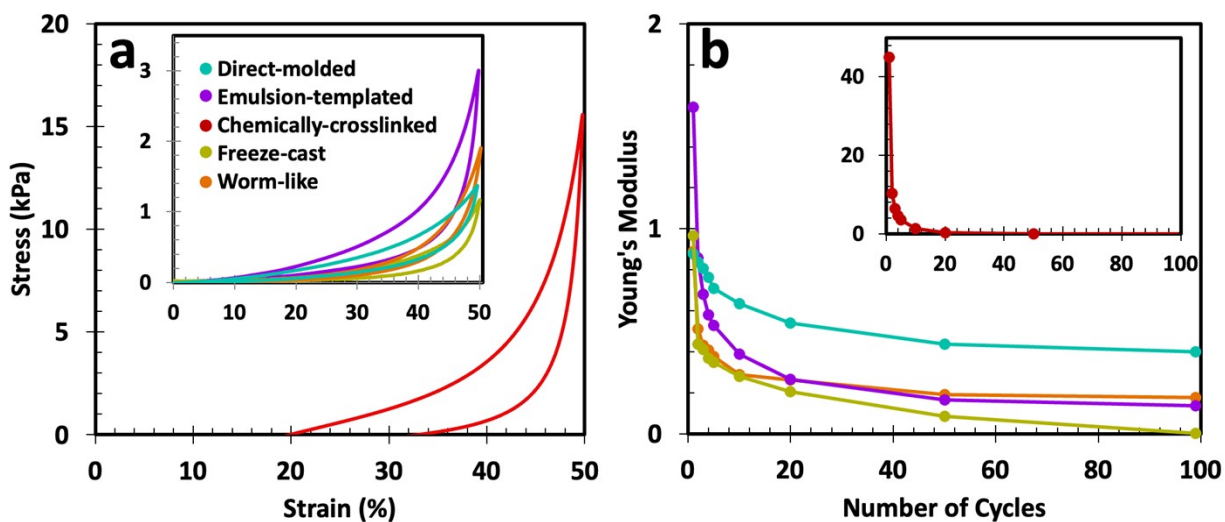
Figure S17. (a) A comparison of the stress-strain curves of the cryogels at a maximum strain of 50% at cycle 50. (b) The Young's modulus, calculated from the initial slope of the unloading stress-strain curves over repeated cycles, shows some degree of residual deformation.
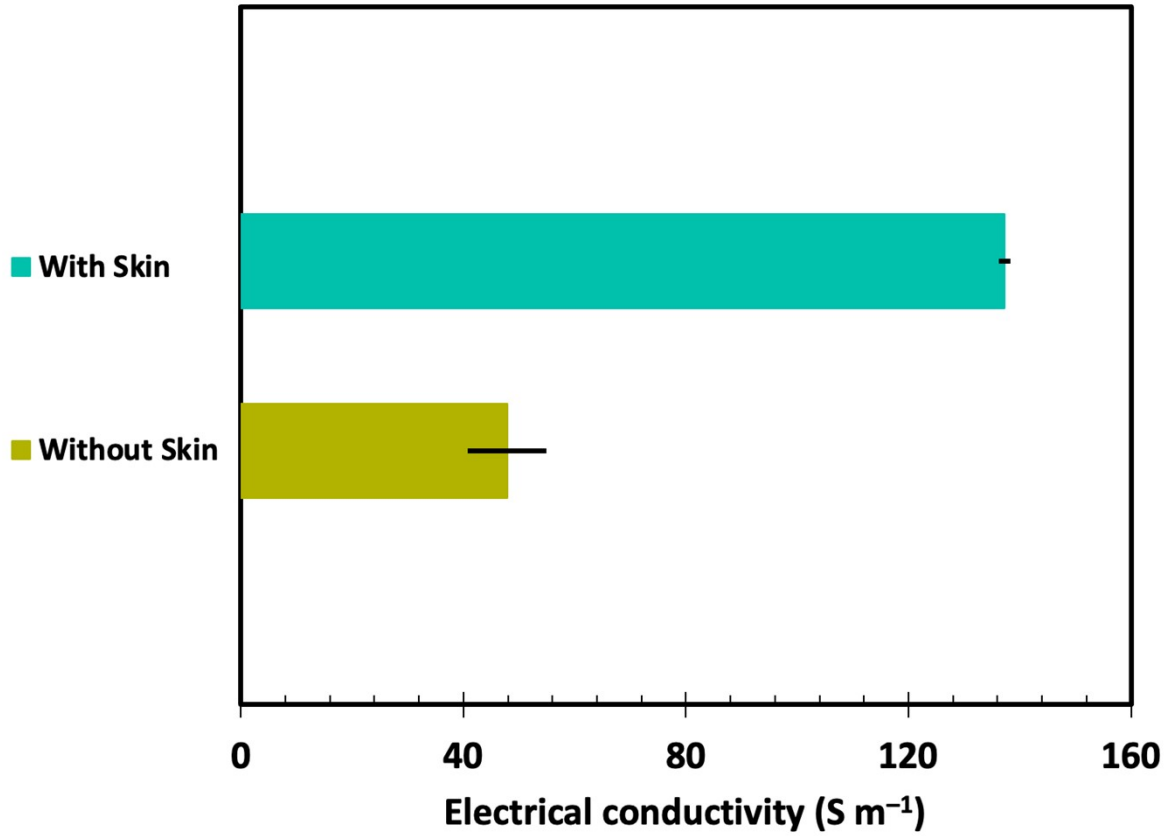
Figure S18. The chemically-crosslinked cryogels exhibit higher electrical conductivity, attributed to the skin formed around the interconnected core. The skin was removed using a blade to compare the electrical conductivity with/without skin. All error bars represent the standard deviation.
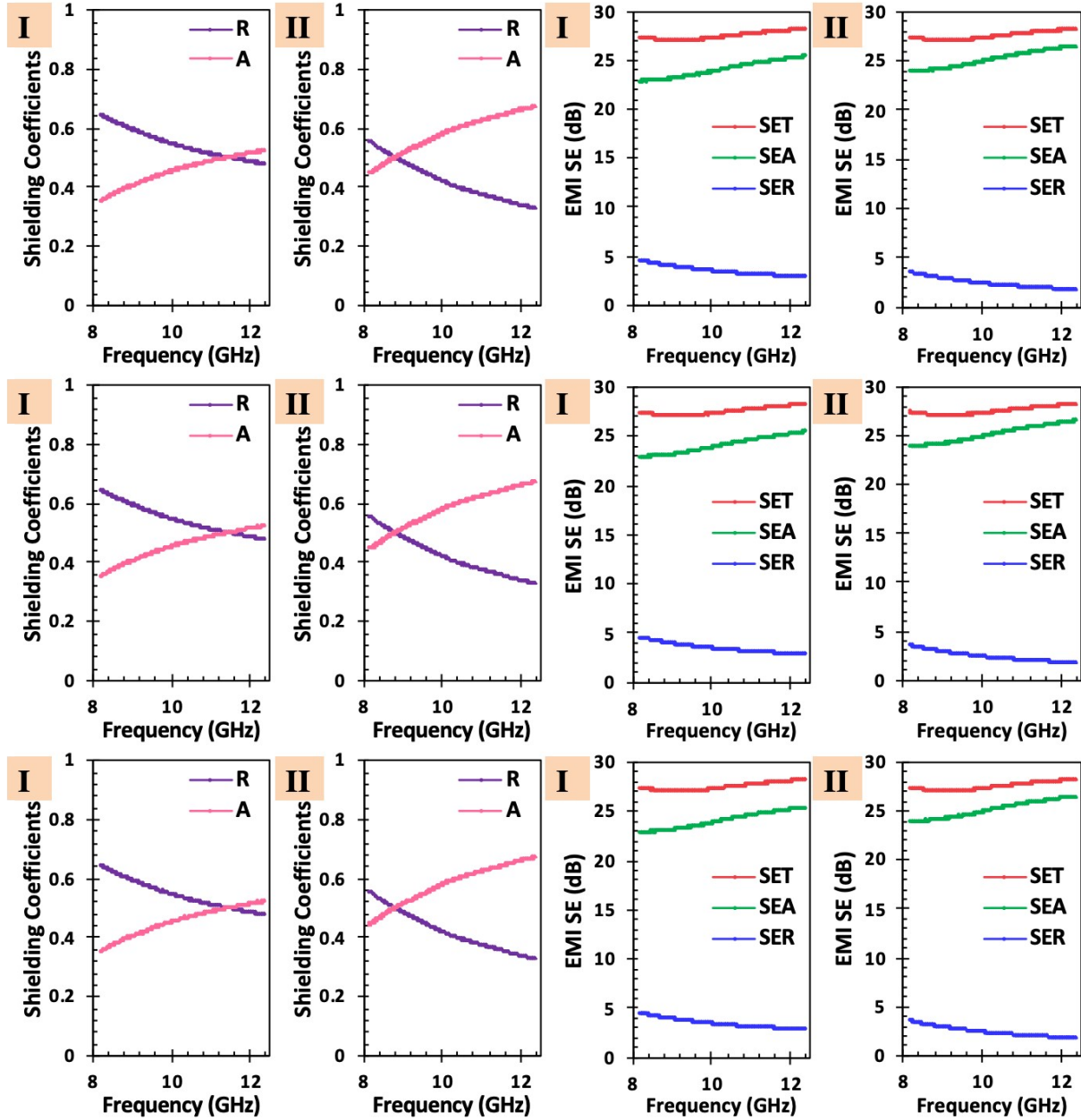
Figure S19. EMI shielding characteristics of reduced graphene-based cryogels fabricated through direct molding. (I) and (II) refer to the data obtained from two different sides of the samples. The thickness of these samples was ~6.91 mm. The VNA was used to measure the scattering parameters three times for each sample.
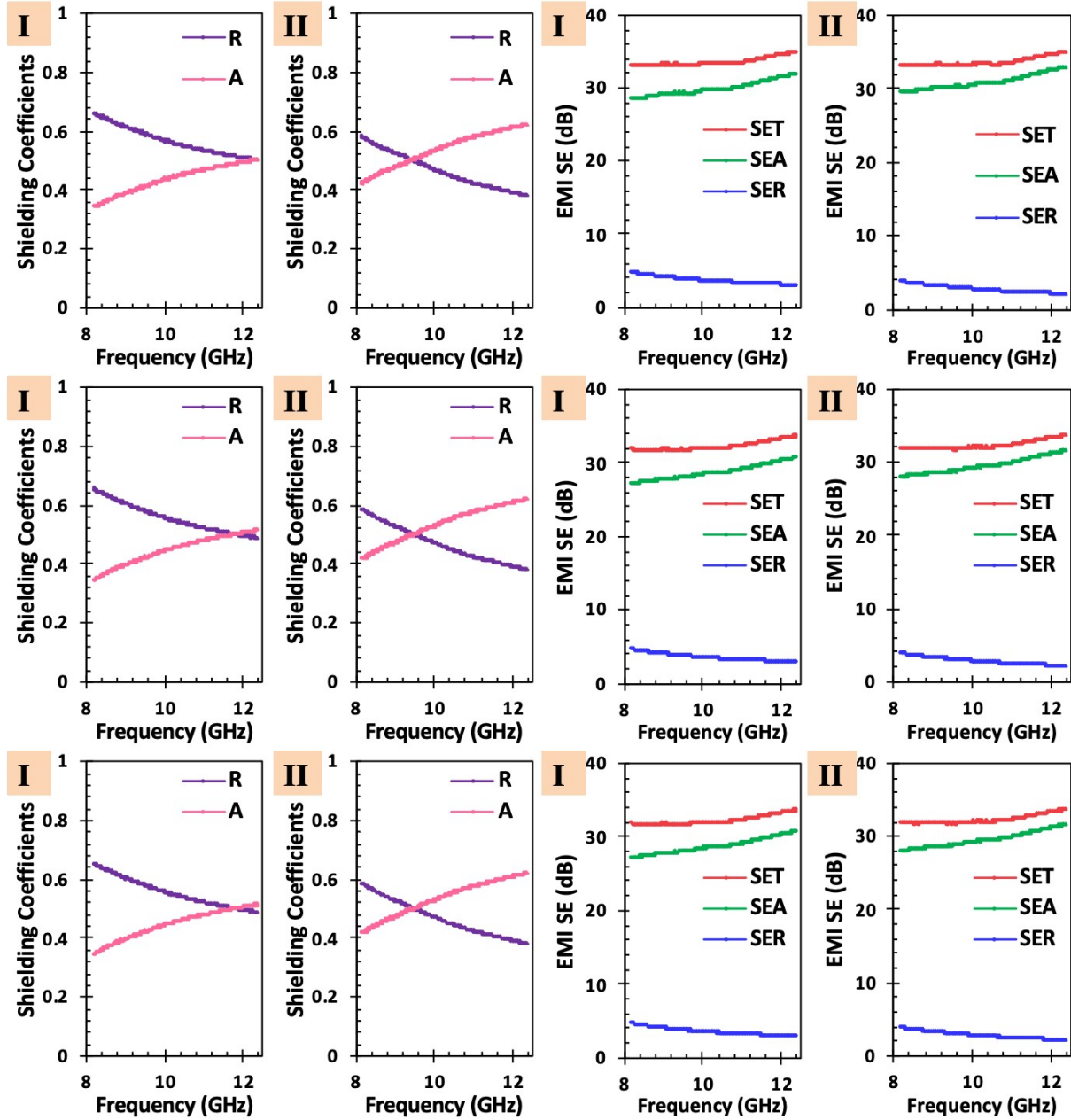
Figure S20. EMI shielding characteristics of reduced graphene-based cryogels fabricated through emulsion templating. (I) and (II) refer to the data obtained from two different sides of the samples. The thickness of these samples was ~7.16 mm. The VNA was used to measure the scattering parameters three times for each sample.
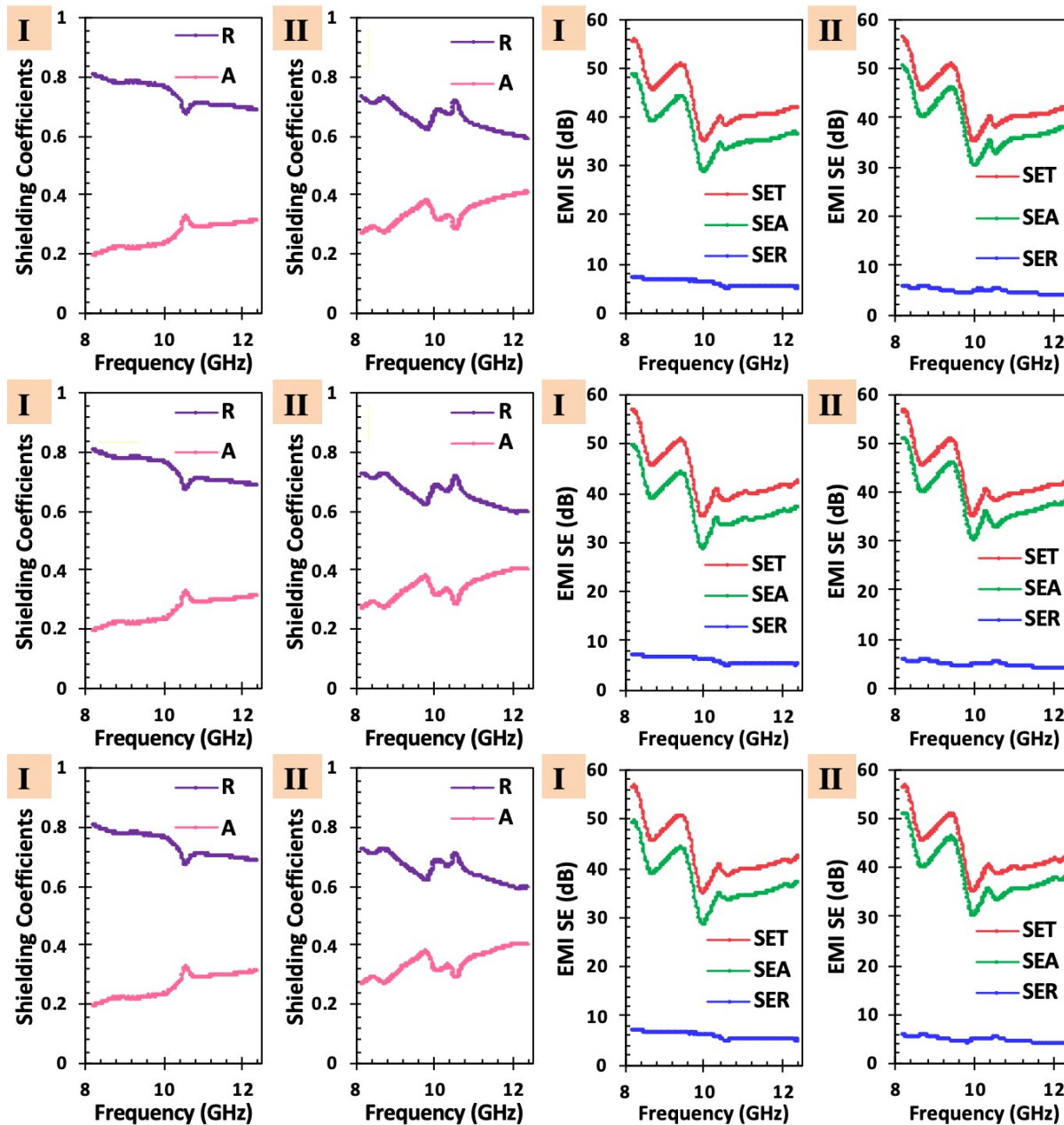
Figure S21. EMI shielding characteristics of reduced graphene-based cryogels fabricated through chemically-induced gelation. (I) and (II) refer to the data obtained from two different sides of the samples. The thickness of these samples was ~8.05 mm. The VNA was used to measure the scattering parameters three times for each sample.
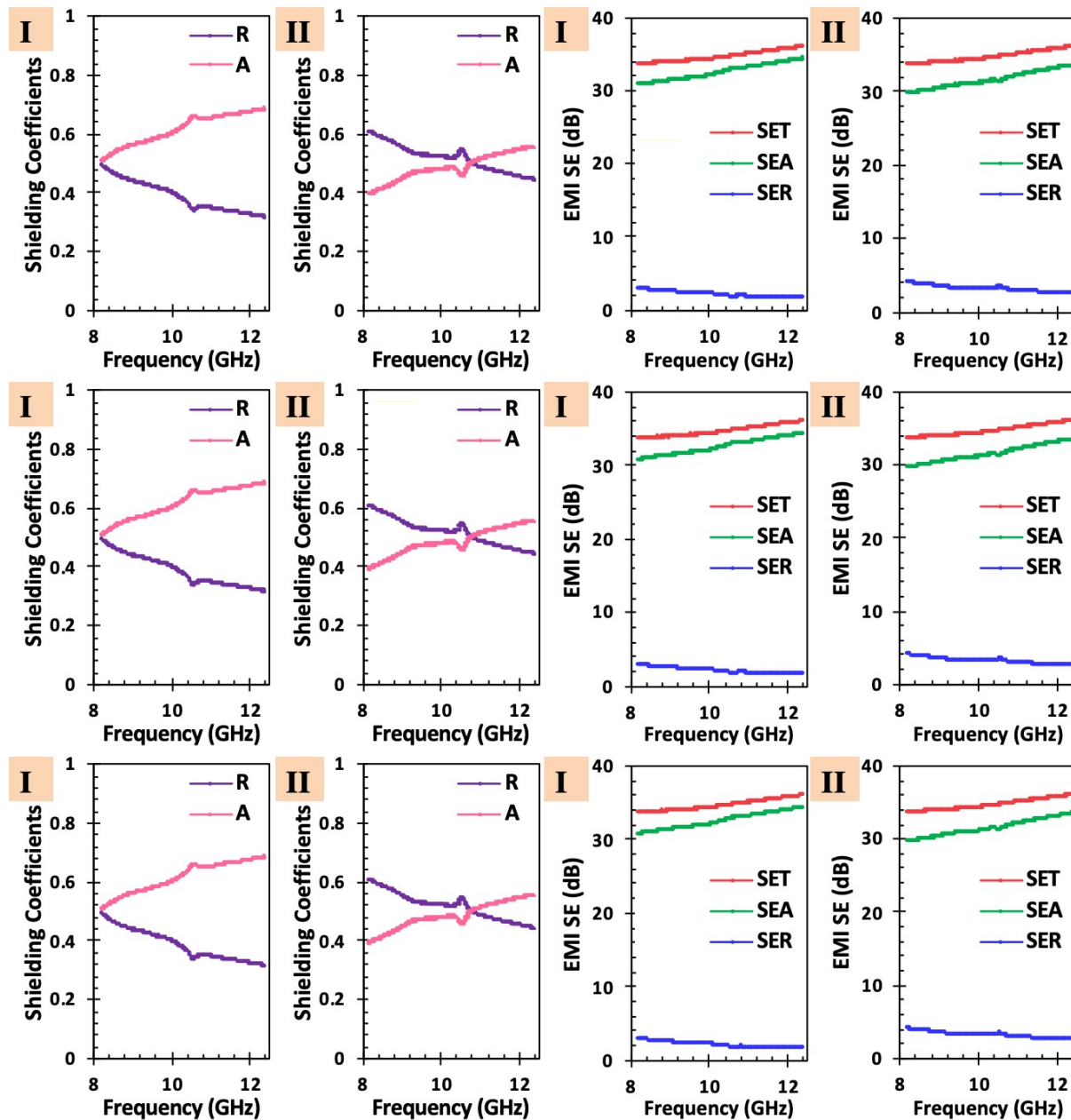
Figure S22. EMI shielding characteristics of reduced graphene-based cryogels fabricated through Freeze-casting. (I) and (II) refer to the data obtained from two different sides of the samples. The thickness of these samples was ~6.80 mm. The VNA was used to measure the scattering parameters three times for each sample.
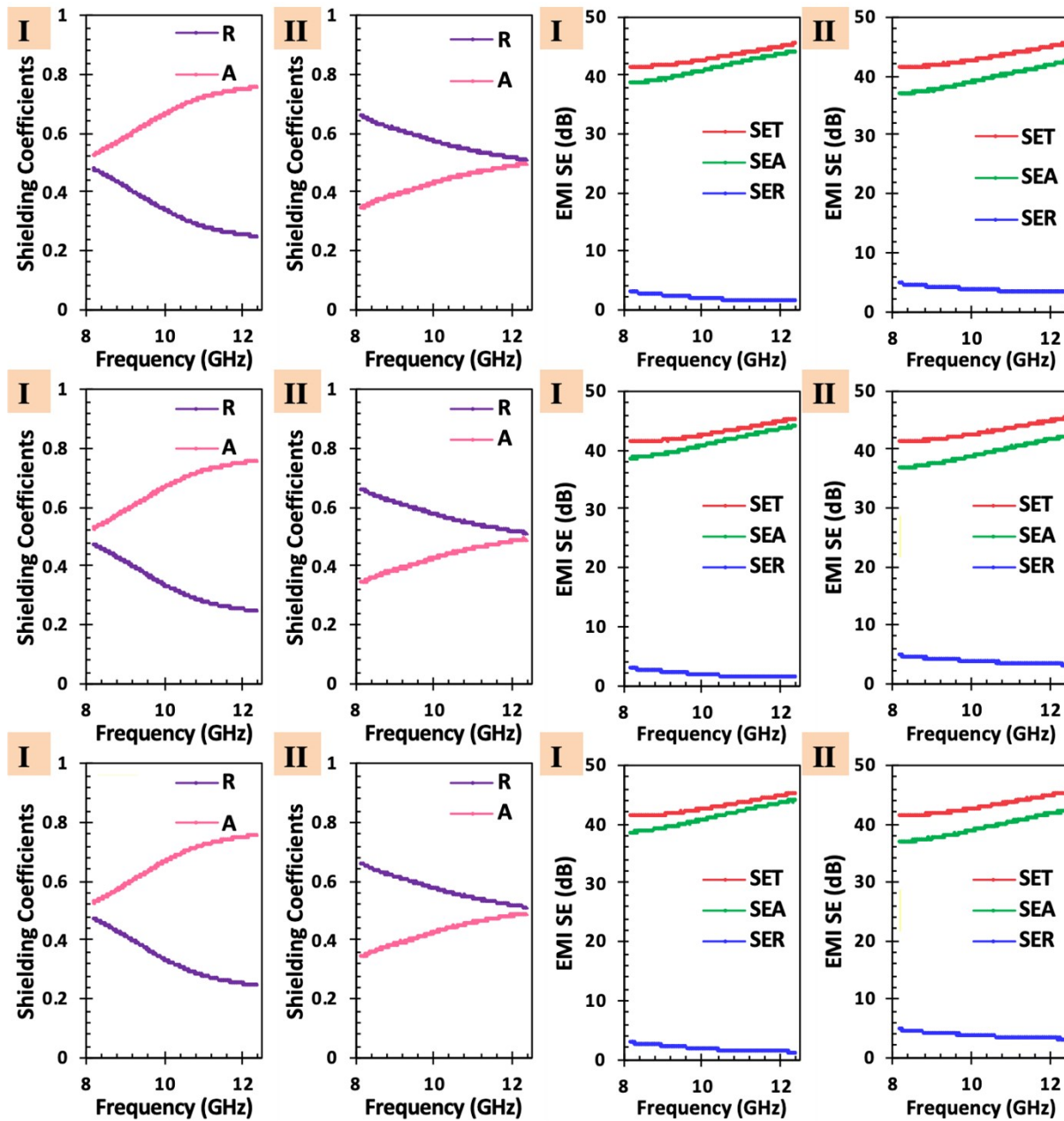
Figure S23. EMI shielding characteristics of reduced graphene-based cryogels fabricated through interfacial assembly. (I) and (II) refer to the data obtained from two different sides of the samples. The thickness of these samples was ~6.74 mm. The VNA was used to measure the scattering parameters three times for each sample.

Table S1. A comparison of the electrical conductivity, shielding efficiency, density, A, and SSE/t of the fabricated cryogels.

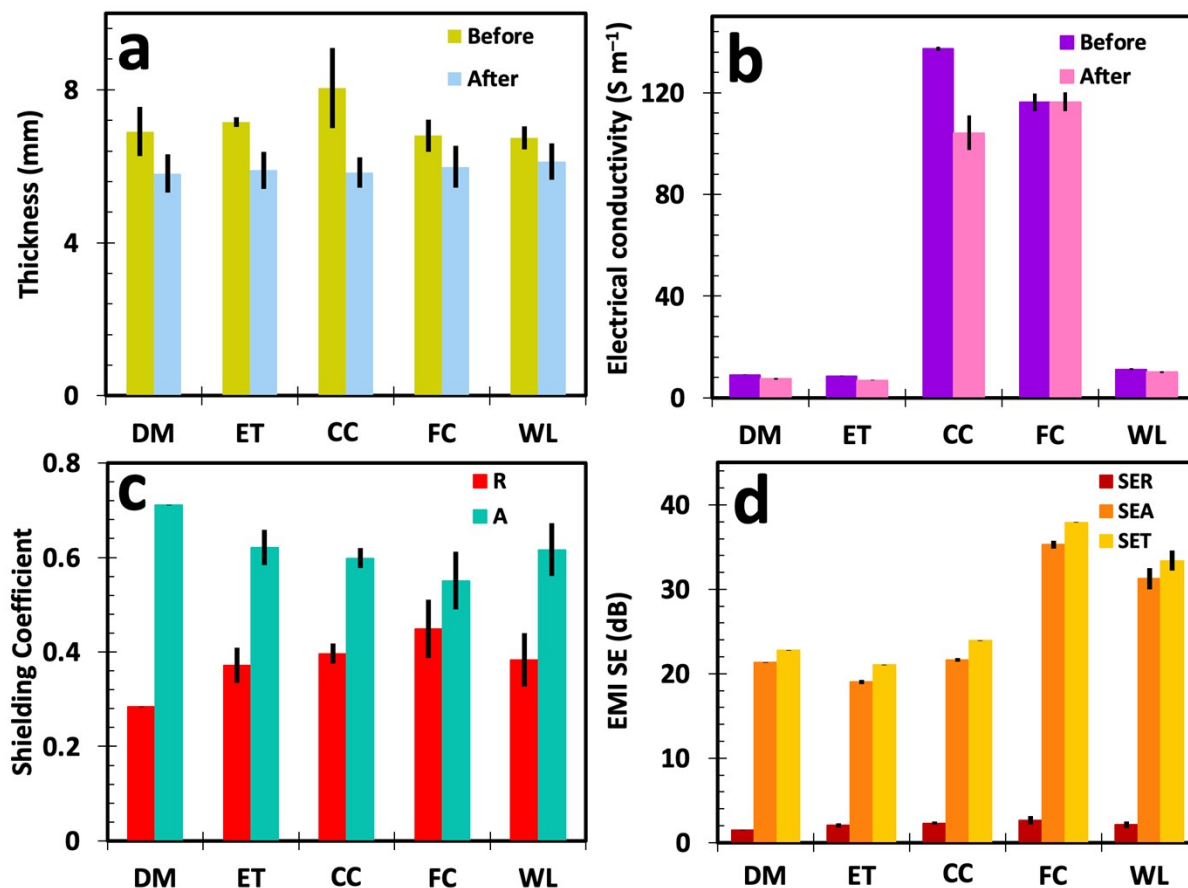| Fabrication Method	Thickness (mm)	Electrical Conductivity (S m^{-1})	EMI SE (dB)	Density (mg cm^{-3})	A	SSE/t (dB cm^2 g^{-1})
Direct Molding	6.91	9.15	27.50	4.48	0.52	8881.95
Emulsion Templating	7.16	8.67	32.58	4.09	0.49	11147.75
Chemically-induced Gelation	8.05	137.28	43.17	4.54	0.30	11824.33
Freeze-casting	6.80	116.24	34.68	4.43	0.55	11521.08
Liquid Streaming	6.74	11.31	42.92	2.47	0.55	25802.50

Figure S24. (a) A comparison of the thickness and (b) electrical conductivity of the cryogels before and after being compressed up to 50% strain over repetitive cycles. (c-d) EMI shielding characteristics of the corresponding cryogels. All error bars in (a-b) represent the standard deviation. The abbreviations DM, ET, CC, FC, and WL correspond to direct-molded, emulsion-templated, chemically-crosslinked, unidirectional freeze-cast, and worm-like cryogels, respectively.
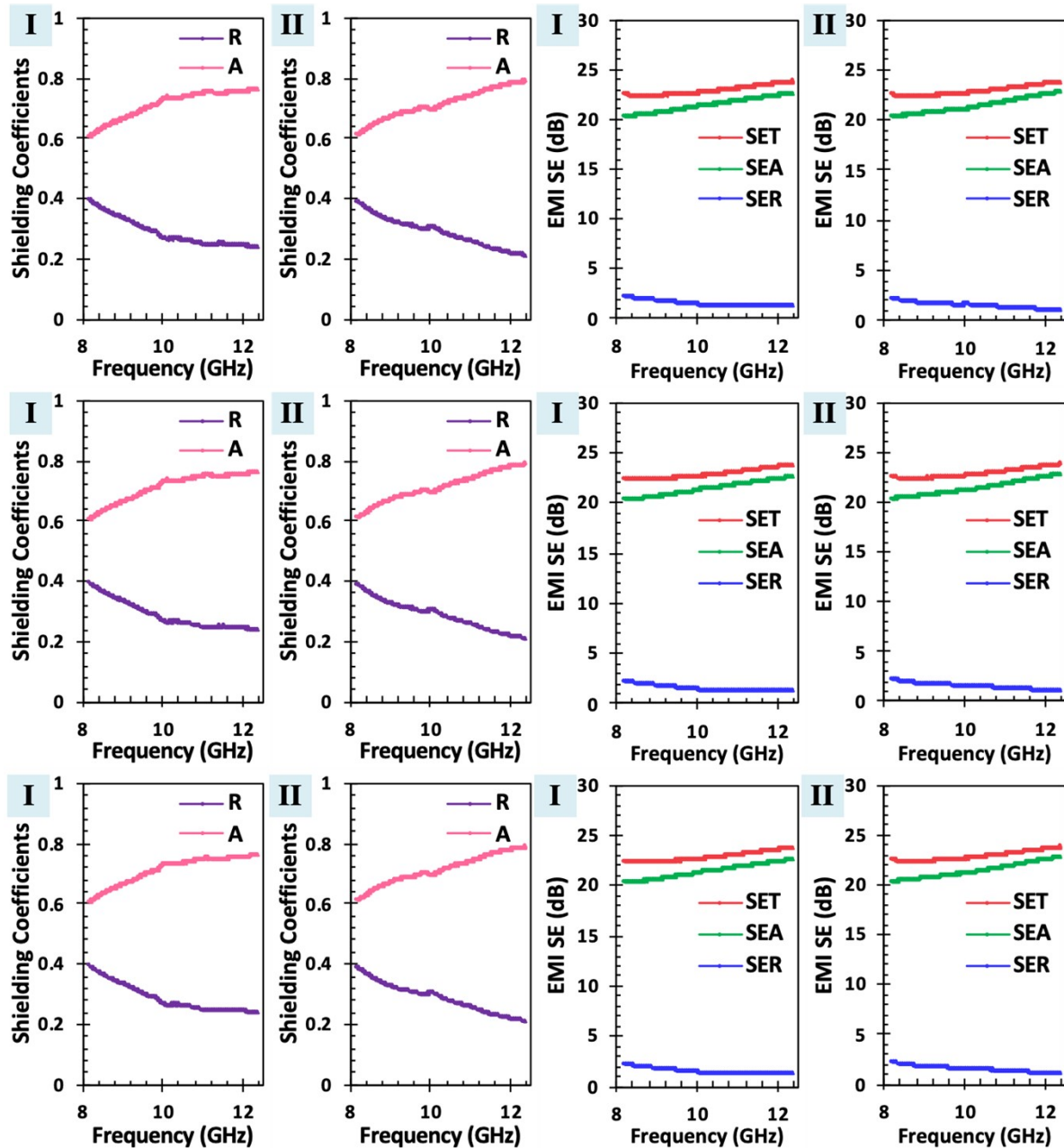
Figure S25. EMI shielding characteristics of direct-molded cryogels after compression. (I) and (II) refer to the data obtained from two different sides of the samples. The thickness of these samples was ~5.80 mm. The VNA was used to measure the scattering parameters three times for each sample.
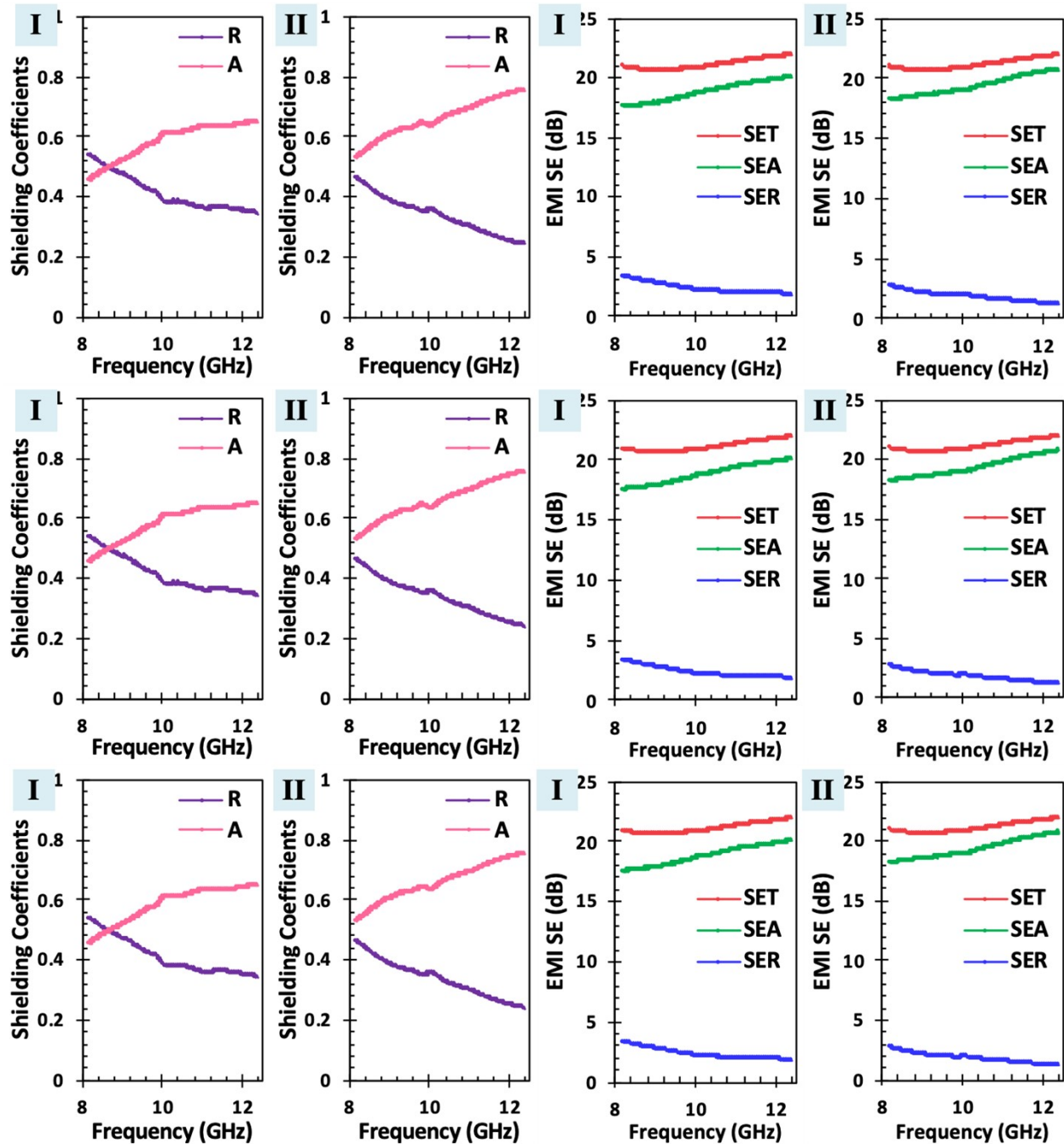
Figure S26. EMI shielding characteristics of emulsion-templated cryogels after compression. (I) and (II) refer to the data obtained from two different sides of the samples. The thickness of these samples was ~5.90 mm. The VNA was used to measure the scattering parameters three times for each sample.
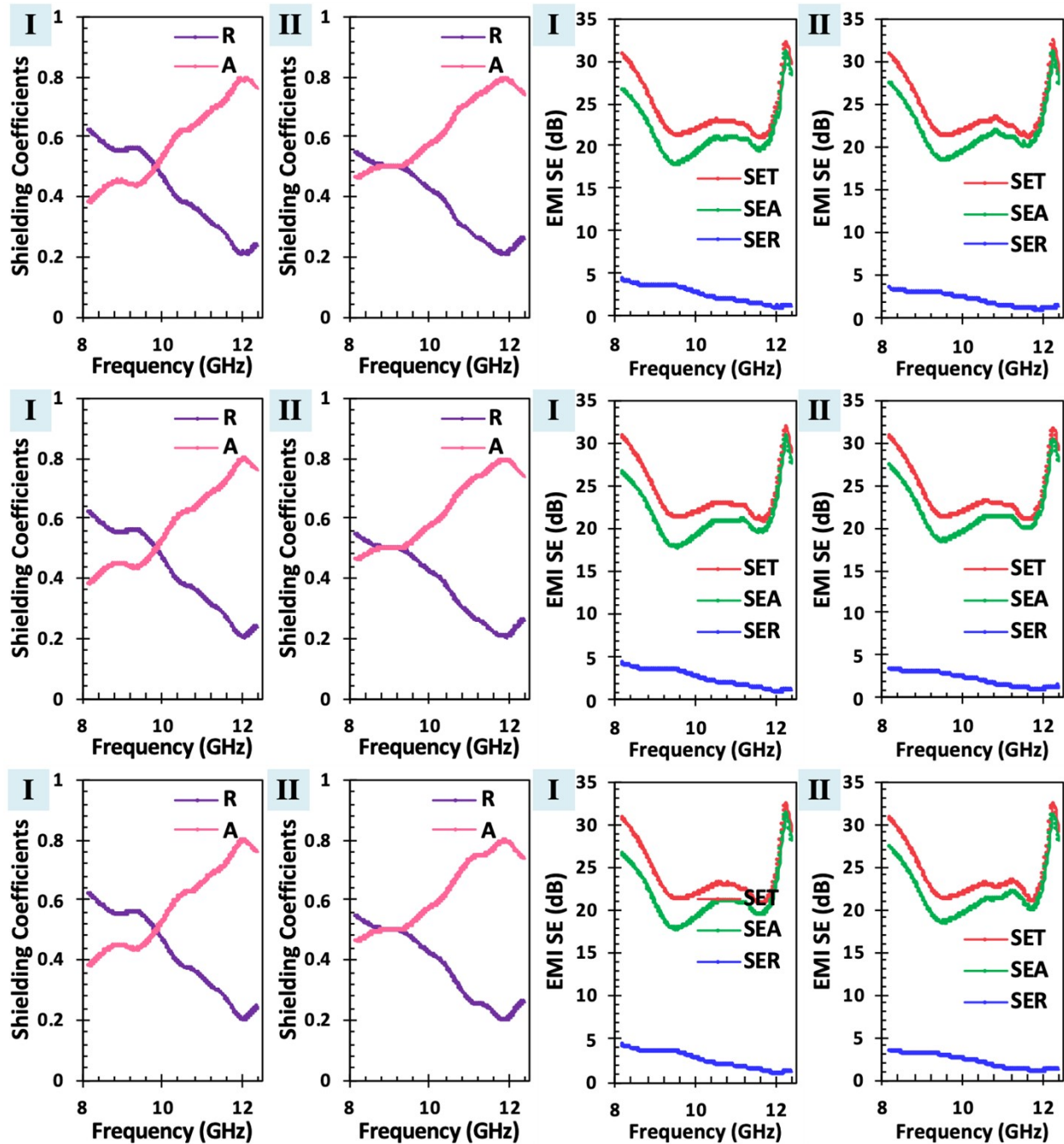
Figure S27. EMI shielding characteristics of chemically-crosslinked cryogels after compression. (I) and (II) refer to the data obtained from two different sides of the samples. The thickness of these samples was ~5.84 mm. The VNA was used to measure the scattering parameters three times for each sample.
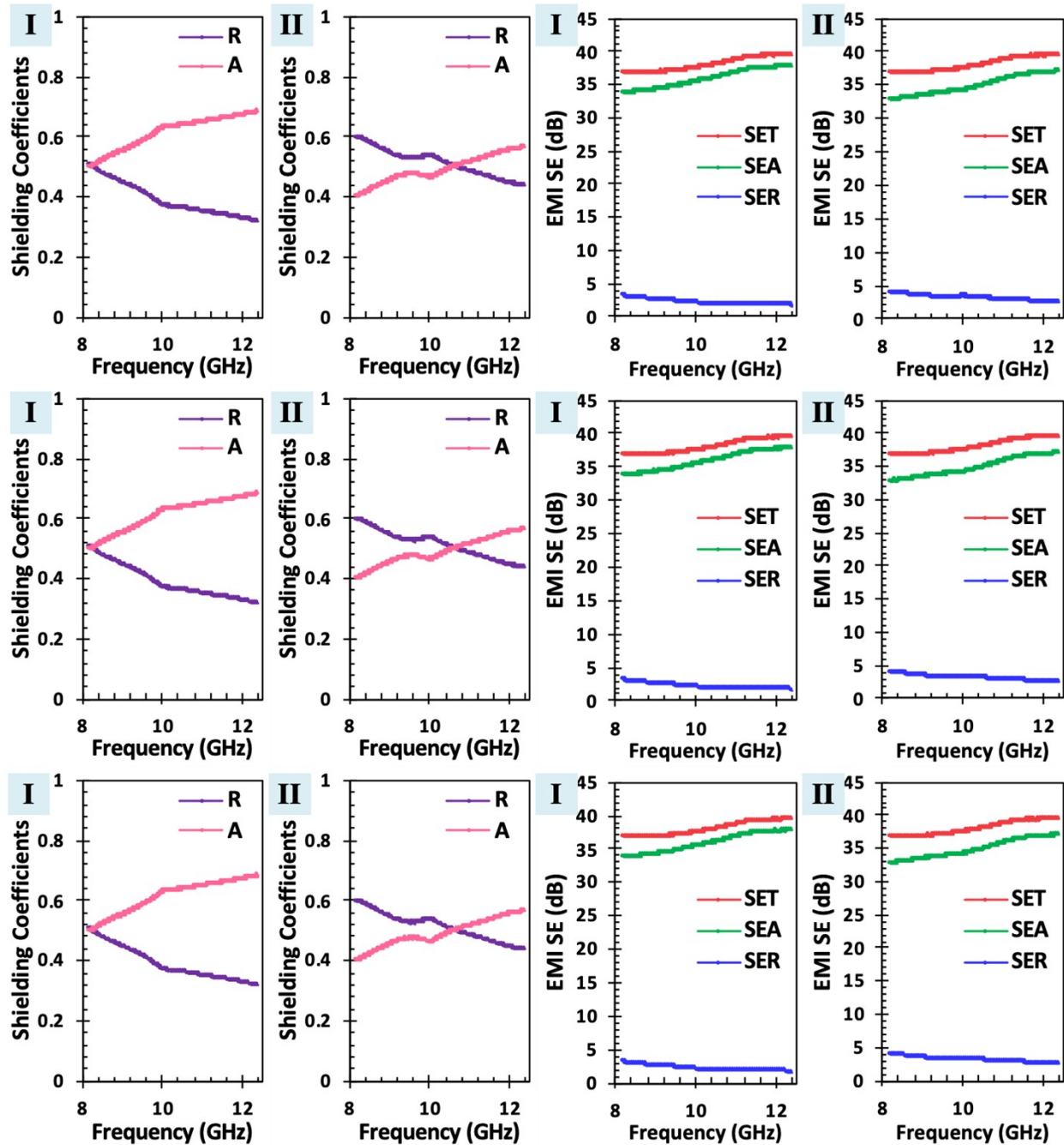
Figure S28. EMI shielding characteristics of freeze-cast cryogels after compression. (I) and (II) refer to the data obtained from two different sides of the samples. The thickness of these samples was ~5.99 mm. The VNA was used to measure the scattering parameters three times for each sample.
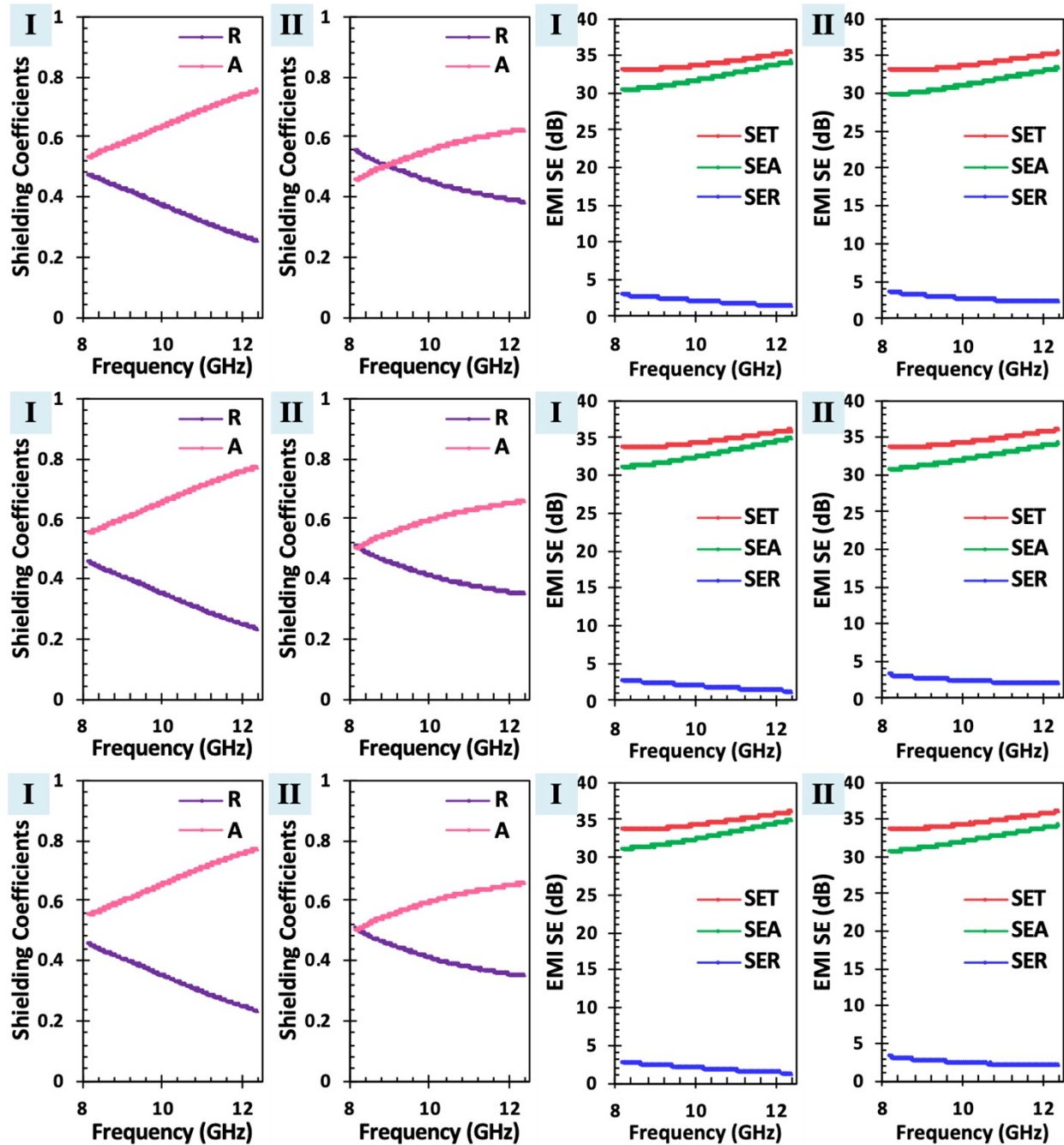
Figure S29. EMI shielding characteristics of worm-like cryogels after compression. (I) and (II) refer to the data obtained from two different sides of the samples. The thickness of these samples was ~6.11 mm. The VNA was used to measure the scattering parameters three times for each sample.

References

1. M. Aswathi, A. V. Rane, A. Ajitha, S. Thomas and M. Jaroszewski, *Advanced Materials for Electromagnetic Shielding: Fundamentals, Properties, and Applications*, 2018, 1-9.

2. A. Ghaffarkhah, S. A. Hashemi, F. Ahmadijokani, M. Goodarzi, H. Riazi, S. E. Mhatre, O. Zaremba, O. J. Rojas, M. Soroush and T. P. Russell, *Nature Communications*, 2023, **14**, 7811.

3. M. Kamkar, A. Ghaffarkhah, R. Ajdary, Y. Lu, F. Ahmadijokani, S. E. Mhatre, E. Erfanian, U. Sundararaj, M. Arjmand and O. J. Rojas, *Small*, 2022, **18**, 2200220.

4. A. M. Nair, S. M. Zachariah and S. Thomas, *Qeios*, 2022.

5. B. Shen, Y. Li, W. Zhai and W. Zheng, *ACS Applied Materials & Interfaces*, 2016, **8**, 8050-8057.

6. A. Iqbal, P. Sambyal and C. M. Koo, *Advanced Functional Materials*, 2020, **30**, 2000883.

7. H. W. Ott, *Electromagnetic Compatibility Engineering*, John Wiley & Sons, 2011.

8. Q. Li, L. Chen, J. Ding, J. Zhang, X. Li, K. Zheng, X. Zhang and X. Tian, *Carbon*, 2016, **104**, 90-105.

9. M. Han, X. Yin, K. Hantanasirisakul, X. Li, A. Iqbal, C. B. Hatter, B. Anasori, C. M. Koo, T. Torita and Y. Soda, *Advanced Optical Materials*, 2019, **7**, 1900267.

10. S. H. Lee, S. Yu, F. Shahzad, W. N. Kim, C. Park, S. M. Hong and C. M. Koo, *Nanoscale*, 2017, **9**, 13432-13440.

11. B. Anasori and Û. G. Gogotsi, *2D Metal Carbides and Nitrides (MXenes)*, Springer, 2019.

12. R. B. Schulz, V. C. Plantz and D. R. Brush, *IEEE Transactions on Electromagnetic Compatibility*, 1988, **30**, 187-201.

13. M. González, J. Pozuelo and J. Baselga, *The Chemical Record*, 2018, **18**, 1000-1009.